J. Fluid Mech. (1972), *vol.* 52, *part* 1, *pp.* 57–95
Printed in Great Britain

An experimental and analytical study of natural convection with appreciable thermal radiation effects

By T. AUDUNSON† AND B. GEBHART
Department of Thermal Engineering, Cornell University

(Received 26 January 1971 and in revised form 2 August 1971)

An experimental and theoretical investigation has been carried out to determine the effect of thermal radiation on a natural convection boundary layer formed adjacent to a vertical flat surface with uniform heat flux input. In the experiment, the gases air, argon and ammonia were used as the fluid medium, thus permitting the observation of radiation effects in non-abosrbing and absorbing media. Experimental results were obtained for three different wall emittances at ambient pressures ranging from 2 to 8 atmospheres in air and argon and from 2 to 7 atmospheres in ammonia. An interferometer was used to measure the temperature distributions in the boundary layer and to evaluate the conductive (convective) heat flux from the surface into the fluid medium. The experimental temperature distributions and heat-transfer results obtained in ammonia gas are compared to the predictions of a perturbation analysis developed by the present writers. General agreement between theory and experiment is found. The presence of a radiating gas is seen to increase the convective heat transfer by as much as 40 % for the conditions of the present experiments. The results further indicate that the temperature distributions and wall-temperature gradients are strongly affected by both variations in the surface emittance and variations in gaseous emission and absorption. For non-absorbing gases, the experimental results are found to be in general agreement with existing theory. It is also shown that the experimental temperature distributions agree very well with theoretical predictions obtained by treating the convection and radiation processes as independent and superimposed.

1. Introduction

This paper concerns the transfer of heat by natural convection, diffusion and radiation, at moderate temperatures, where the fluid itself may actively participate in the radiation transfer. Even at moderate temperatures and densities, radiation effects may be important for gases such as water vapour, ammonia and carbon dioxide. This study was undertaken to gain some general understanding of the effect of radiation interaction on temperature distribution and heat transfer in a natural convection flow, through an analytically guided interpretation of accurate experimental results.

Specifically, we shall consider laminar natural convection flow adjacent to a

† Present address: River and Harbour Laboratory at the Technical University of Norway, Trondhjem.

vertical flat surface in both absorbing and non-absorbing gases. We shall be concerned with the low level of temperature characteristic of environmental processes. The use of ammonia at elevated pressures simulates, on a laboratory scale, the spatially more extensive and lower concentration level processes of usual interest.

Experimental heat-transfer results and temperature distributions are obtained by interferometry. For the non-absorbing gases, air and argon, the experimental findings are compared with the theoretical predictions set forth by Cess (1964*b*). The radiation effect in this circumstance is entirely in the modification of surface-boundary conditions. Experimental temperature and heat-transfer data are also obtained with an absorbing gas (NH_3) at pressures from 2–7 atm. These results are compared to our own analysis of the boundary-layer equations; the radiation interaction is incorporated by a perturbation method. The first term in the expansion represents the solution without radiation, higher terms correcting for radiation effects. The solution is obtained by dividing the flow field into an inner and outer region. Energy transport in the inner region includes convection, diffusion and radiation, whereas the outer region transport mechanisms are principally radiation and convection. The regions are joined by matching. The technique of analysis is therefore similar to the one employed by Cess (1964*a*) in forced flow, although the mechanisms of buoyancy induced flow and transport are quite different. All experimental measurements were at a fixed location along the various test surfaces and changes in the different parameters characterizing the transport processes were obtained by changing the ambient pressure level in the range of 2 to a maximum of 8 atmospheres. Also, three different surface conditions were used so that the effect of varying surface emittance (using the values 0·2, 0·5, 0·8) may be observed.

The general problem of radiation interaction with other modes of heat transfer has received extensive analytical study, principally as a result of particular needs in technology. However, because of the analytical complexity of transport processes involving radiation transfer, simplifying approximations very often are made. Few experimental verifications of the analytical predictions are available however. Tien (1968) presented a review of the different analytical approximations and models commonly used to describe radiation characteristics of gases. The review also gave a detailed summary of measured and calculated values of radiation emission and absorption properties for a number of different gases.

Gille & Goody (1964) studied the effect of infra-red gas emission and absorption on the onset of thermal instability in a stationary horizontal gas layer heated from below. A non-grey analysis was used and the accompanying experimental data are in general agreement with the theoretical results. Their investigation also employed the gases air and ammonia. As in our investigation, temperature data were obtained by interferometry. The authors found that the critical Rayleigh number for thermal instability may be much higher in ammonia than in air.

Radiation interaction with a forced flow has been extensively studied. Viskanta (1966) presented a review of investigations of radiation interaction with convective transport processes. His review article reported a total absence of ex-

perimental studies of infra-red radiation interaction with laminar forced flow. To the knowledge of the present writers this is still true.

Cess (1964*b*) presented the first investigation of radiation interaction with a natural convection flow. He considered the particular circumstance of natural convection flow of a non-absorbing gas along a vertical flat surface. In this circumstance one considers the effect of the surface radiative flux upon the surface and boundary-layer temperature distribution and upon the convective heat-transfer rates.

England & Emery (1969) have presented the only experimental investigation of thermal radiation effects on the laminar natural convection boundary layer in an absorbing and emitting gas. They studied the flow adjacent to a heated vertical flat plate. A finite-difference technique was used to analyse the equations, and numerical solutions and experimental results for air and carbon dioxide were presented. Their experimental technique, however, leaves doubt about the accuracy of the measured results. No heat-transfer data is given for the absorbing gas and the heat-transfer data for air show wide scatter. They found that the effect of gaseous radiation was small for the conditions of their study.

The problem of radiation interaction in a natural convection flow along a vertical flat plate at constant temperature has been considered analytically in two publications. Cess (1966) used a singular perturbation approach to the problem, in principle similar to his (1964*a*) publication related to the equivalent forced-flow case. The gas was assumed grey and the flow generating surface was assumed black. Arpaci (1968) used an integral analysis technique for the same problem, and considered both the optically thick and the optically thin limit. Results for surface emissivities different from one was only given for the optically thick boundary layer.

The constant heat-flux wall condition and the effect of varying surface emittance studied in the present experiment, however, makes the above results inapplicable for comparison with our results.

2. Analysis

The physical model and co-ordinate system are illustrated in figure 1. The conservation equations for mass, momentum and energy are well known and will not be developed here. The presence of radiation will not alter the equations for mass and momentum conservation; the effect appears as an additional term in the energy equation. It is conceivable that the radiation could cause an extremely thick boundary layer (particularly the outer radiation layer) which would invalidate the boundary-layer approximations. In the present analysis, however, the boundary-layer approximations have been employed. Our experimental observations indicate that this regime does, in fact, apply for the conditions relevant to this study. The usual Boussinesq approximations, along with other permissible ones (see Gebhart 1971), have also been employed. Since the accompanying experimental study was to be at a moderate temperature level with small differences, uniform transport properties may be assumed. The

steady-state mass, momentum and energy conservation equations then take the form:

$$\frac{\partial u}{\partial x}+\frac{\partial v}{\partial y}=0, \tag{1}$$

$$u\frac{\partial u}{\partial x}+v\frac{\partial u}{\partial y}=\nu\frac{\partial^2 u}{\partial y^2}+g\beta\Delta t, \tag{2}$$

$$\rho c_p\left(u\frac{\partial t}{\partial x}+v\frac{\partial t}{\partial y}\right)=k\frac{\partial^2 t}{\partial y^2}-\frac{\partial}{\partial y}(q_{ry}). \tag{3}$$

In these equations x and y are the longitudinal and normal co-ordinates, u and v refer to the longitudinal and normal velocity components and t is the local temperature of the fluid medium. The normal component of the net radiation

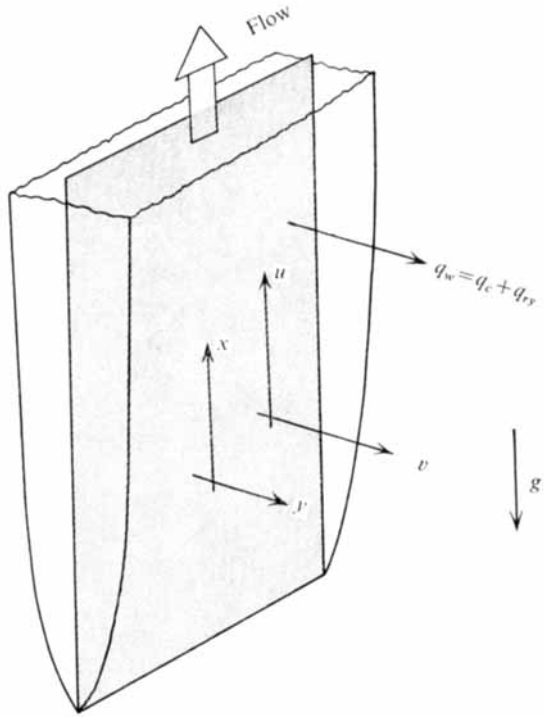

FIGURE 1. Definition of physical model and co-ordinate system.

flux is q_{ry}, ρ is the fluid density, ν is the kinematic viscosity, k is the thermal conductivity, c_p is the specific heat, β is the coefficient of thermal volumetric expansion and g is the local gravitational acceleration. In addition to the above approximations, it has been assumed that the divergence of the radiation flux in the longitudinal direction can be neglected compared with that in the normal direction. According to Cess (1964*a*) this is justified if $U_c x/(16\sigma T_0^3/3\kappa\rho c_p) \gg 1$ [typically $O(10^2$–$10^3)$ for the present experiment], where U_c is the characteristic convection velocity in the boundary layer, σ is Planck's constant, T_0 is the absolute temperature of the ambient fluid and κ is a radiation absorption constant of the fluid medium. This condition is obtained by comparing the longitudinal

convection term with the longitudinal divergence of the radiation flux, using the Rosseland approximation for radiation flux. This assumption of one-dimensionality becomes inaccurate for gases having intermediate and large values of the radiation absorption length.

In addition to the assumptions already made the gas will be assumed to be grey and non-scattering. The boundary layer is assumed optically thin and the surface generating the natural convection flow is assumed to be a diffuse emitter and reflector. The radiation term in the energy equation will be treated as a perturbation of the natural convection flow without radiation interaction. As will be shown later, the experimental temperature differences are small, thus permitting linearization of the radiation term.

2.1. *Development of perturbation parameters*

Each term of (3) may be written in terms of characteristic quantities as follows:

$$\text{Convection term} = \rho c_p U_c \Delta t_c / x, \tag{3a}$$

$$\text{Diffusion term} = k \Delta t_c / \delta^2, \tag{3b}$$

$$\text{Radiation term} = 2\sigma T_0^3 \Delta t_c \kappa_p. \tag{3c}$$

The characteristic boundary-layer thickness is $\delta = x/(\frac{1}{5}Gr^*)^{\frac{1}{5}} = x/G^*$, where $Gr^* = q_w x^4 g\beta/k\nu^2$ and q_w refers to the wall heat flux. One should note that the G^* defined above differs by a fraction of $\frac{1}{5}$ from the usual definition of G^* (Gebhart 1971). Comparing the terms (3*a*) and (3*c*) one obtains the perturbation parameter for radiation absorption

$$\zeta = \frac{2\sigma T_0^3 \kappa_p x}{\rho c_p U_c} = \frac{2\sigma T_0^3 \kappa_p x}{\rho c_p (5\nu/x)\, G^{*2}}, \tag{4}$$

where the estimate of the convection velocity U_c is that which applies for moderate Prandtl numbers for a uniform heat flux vertical surface in the absence of radiation (Sparrow & Gregg 1956). The radiation term is estimated from the usual expression for the optically thin limit of the divergence of the one-dimensional radiation flux as follows:

$$\partial(q_{ry})/\partial y = -2\sigma\kappa_p[(T_w^4 - T_0^4) - 2(T^4 - T_0^4)] \simeq 8\sigma T_0^3 \kappa_p \Delta t_c,$$

where Δt_c is the characteristic temperature of the flow field, κ_p is the Planck mean absorption coefficient, and T and T_w are the absolute temperatures in the boundary layer and at the surface.

Of particular interest here, because of the experiment to which the results are to be compared, is a vertical flat surface with a uniform net heat-flux surface condition. Including surface emission modifies the boundary condition and makes the resulting flow circumstance non-similar.

At $y = 0$ one has for the temperature gradient:

$$\frac{\partial t}{\partial y} = -\frac{q_w}{k} + \frac{q_{ry}}{k} \to \frac{\partial}{\partial \eta}\left(\frac{t}{\Delta t_c}\right) = -\frac{q_w \delta}{k \Delta t_c} + \frac{\delta}{k \Delta t_c} q_{ry},$$

where $\eta = y/\delta$. The radiation flux may be estimated as

$$q_{ry} = \epsilon\sigma(T_w^4 - T_0^4) = 4\epsilon\sigma T_0^3 \Delta t_c.$$

By comparing the conduction and radiation terms in the above expression the following additional perturbation parameter arises:

$$\xi = \frac{\sigma T_0^3 \epsilon \Delta t_c}{q_w} = \frac{\sigma T_0^3 \epsilon x}{kG^*}, \tag{5}$$

where ϵ is the emittance of the heated surface. The expression for $\Delta t_c = q_w x/kG^*$ is the characteristic temperature for the natural convection boundary-layer flow, subject to a uniform heat flux boundary condition, as presented by Sparrow & Gregg (1956).

It should be noted that there is, from (4) and (5), a simple relationship between the two parameters, namely

$$\xi = (5Pr\,\epsilon/2\kappa_p\delta)\,\zeta, \tag{6}$$

where Pr is the Prandtl number of the fluid medium.

2.2. *Delineation of transport regions*

As stated earlier, the radiation interaction phenomenon under investigation will be regarded as a small perturbation of the primary transport processes. The first term in the series expansion of the solution will then represent natural convection flow without any radiation effect. The solution is given as generalized functions in terms of a similarity variable $\eta = y/\delta$, which is of $O(1)$ within the boundary layer. In accordance with the grey-gas formulation we define a non-dimensional distance variable τ for the radiation phenomenon as

$$\tau = \int_0^y \kappa\, dy = \kappa y = \kappa_p y. \tag{7}$$

Hence one can write $$\eta = \tau/\kappa_p\delta.$$

Now, for the optically thin boundary layer $\kappa_p\delta < 1$, which for $\eta = O(1)$ implies $\tau \to 0$ in this domain. Conversely, for $\tau = O(1)$ and $\kappa_p\delta < 1$, $\eta \to \infty$. The solution is thus divided into two domains. The inner region is characterized by $\eta = O(1)$ and $\tau \to 0$ and the outer one by $\tau = O(1)$ and $\eta \to \infty$. The two regions will subsequently be coupled in their asymptotic forms.

2.3. *Outer-region solution*

The flow in the outer region is also regarded as a perturbed flow, where the first term represents the asymptotic form of a non-absorbing convection flow (zero subscript) and following terms correct for the presence of radiation. Primed variables below represent the perturbation quantities. The postulated nature of the outer flow mechanism is further discussed and justified in § 2.5. Thus

$$u = u_0 + u', \quad v = v_0 + v', \quad t = t_0 + t'. \tag{8}$$

In the outer region

$$u_0 = 0, \quad v_0 = -4f_0(\infty)\,(\nu/\delta) \sim U_c(\delta/x), \quad t = t_0.$$

The expression for v_0 is taken from the boundary-layer similarity solution, where $v = -(\nu/x)\,G^*[(4f_0 - \eta f_0')]$ and f_0 is the generalized stream function (see Sparrow & Gregg 1956). For $\eta \to \infty$ one has $v_0 = -(\nu/x)\,G^*.\,4f_0(\infty)$. Substitution of (8) into

(1), (2) and (3) retaining only linear terms of the outer perturbation quantities then yields the following set of equations:

$$\frac{\partial u'}{\partial x}+\frac{\partial v'}{\partial y}=0, \tag{9}$$

$$v_0\frac{\partial u'}{\partial y}=\nu\frac{\partial^2 u'}{\partial y^2}+g\beta t', \tag{10}$$

$$\rho c_p v_0\frac{\partial t'}{\partial y}=k\frac{\partial^2 t'}{\partial y^2}-\frac{\partial}{\partial y}(q_{ry}). \tag{11}$$

Since the ratio between the diffusion and convection terms in the above equations is $O(\kappa_p\delta)$, the temperature and velocity functions of the outer field are expressed as

$$h=t'/\Delta t_c=h^{(0)}+h^{(1)}(\kappa_p\delta)+h^{(2)}(\kappa_p\delta)^2+\ldots \tag{12}$$

and

$$s=u'/U_c=s^{(0)}+s^{(1)}(\kappa_p\delta)+s^{(2)}(\kappa_p\delta)^2+\ldots, \tag{13}$$

where the temperature and velocity functions have been normalized with the characteristic variables of the inner field. Substituting the above expressions for h and s into (10) and (11) respectively and ordering the terms in powers of $\kappa_p\delta$, the first approximation to the equations for the outer field becomes

$$U_c v_0\kappa_p\frac{\partial s^{(0)}}{\partial\tau}=g\beta\Delta T_c h^{(0)}, \tag{14}$$

$$\Delta t_c\rho c_p v_0\kappa_p\frac{\partial h^{(0)}}{\partial\tau}=-\kappa_p\frac{\partial}{\partial\tau}q_{ry}, \tag{15}$$

where (7) has been used to generalize the independent variable y. One notes that the first approximation to the outer temperature distribution is independent of the outer velocity field.

An expression for the radiation flux is needed to solve these equations. The one-dimensional radiation flux from a wall into an infinite radiating medium is expressed as

$$q_{ry}=2\left[\epsilon\sigma T_w^4+2(1-\epsilon)\int_0^\infty\sigma T^4E_2(t)\,dt\right]E_3(\tau)$$
$$+2\left[\sigma\int_0^\tau T^4(\tau-\alpha)\,E_2(\alpha)\,d\alpha-\sigma\int_0^\infty T^4(\beta+\tau)\,E_2(\beta)\,d\beta\right], \tag{16}$$

where the exponential integral function $E_n(x)=\int_0^1 e^{-x/\mu}\mu^{n-2}\,d\mu$. The first two terms in (16) refer to the emitted and reflected radiation from the wall, whereas the difference between the two following integrals represents the net radiative flux emitted by the gas volume at absolute temperature T at any location τ. There is no direct way to evaluate (16) since the temperature appearing in the integrals is not known. However, if one expresses the outer-region temperature, as $T=(T_0+t')$ and $T^4\approx T_0^4(1+4t'/T_0)$ it may be shown that to $O(\xi)$ one may use $T=T_0$ in the integrals of (16). It follows that perturbations of the gaseous

emission in the outer field is being ignored. The radiation flux in the outer region $\tau = O(1)$ may then be expressed as

$$q_{ry} = 8\sigma T_0^3 \epsilon (T_w - T_0) E_3(\tau), \tag{17}$$

and

$$\partial q_{ry}/\partial \tau = -8\sigma T_0^3 \epsilon (T_w - T_0) E_2(\tau). \tag{18}$$

Consistent with the above neglection of temperature gradients in the outer domain, q_{ry} vanishes for $\tau \gg 1$.

Substituting these results into (15) and applying the boundary condition $h(\infty) = 0$ one obtains

$$h \simeq h^{(0)} = -\frac{8\sigma T_0^3}{\rho c_p v_0} \epsilon \phi_{0w} E_3(\tau) = \frac{2\phi_{0w}}{f_0(\infty) Pr} E_3(\tau) \xi, \tag{19}$$

where $\phi_{0w}[= (t_w - t_0)/\Delta t_c]$ is the non-dimensional temperature distribution, evaluated at the wall, for the flow in the absence of radiation.

Because it is quite conceivable that the diffusion term in (11) might contribute terms of $O(\xi, \zeta)$ it is necessary to substitute (12) back into (11), and with the aid of (19) investigate the higher order terms, i.e. $h^{(1)}$. It is found that an additional term must be added to the solution (19). The outer temperature distribution thus becomes

$$h \simeq h^{(0)} = \frac{2\phi_{0w}}{f_0(\infty) Pr} E_3(\tau) \xi + \frac{5}{4} \frac{\phi_{0w} \epsilon}{f_0^2(\infty) Pr} E_2(\tau) \zeta. \tag{20}$$

This solution is to be matched to the inner solution at $\eta \to \infty$, i.e. $\tau \to 0$.

Making use of the above result in (14), the outer velocity distribution may be expressed as

$$\frac{\partial}{\partial \tau} s^{(0)} = -\frac{g\beta \Delta t_c}{v_0 \kappa_p U_c} \frac{2\phi_{0w}}{f_0(\infty) Pr} \left[E_3(\tau) \xi + \frac{5}{8} \frac{\epsilon}{f_0(\infty)} E_2(\tau) \zeta \right], \tag{21}$$

subject to the boundary condition $s(\infty) = 0$. The solution is

$$s^{(0)} = \frac{1}{4 f_0(\infty) \kappa_p \delta} \left[\frac{2\phi_{0w}}{f_0(\infty) Pr} E_4(\tau) \xi + \frac{5}{4} \frac{\phi_{0w} \epsilon}{f_0^2(\infty) Pr} E_3(\tau) \zeta \right]. \tag{22}$$

As with the temperature solution, the result for the velocity is substituted back into (10) to investigate the higher order terms introduced by the diffusion term. It is found that the diffusion term adds three terms to (22). The total result then reads

$$\begin{aligned} s \simeq s^{(0)} = {} & \frac{1}{4 f_0(\infty) \kappa_p \delta} \left[\frac{2\phi_{0w}}{f_0(\infty) Pr} E_4(\tau) \xi + \frac{5}{4} \frac{\phi_{0w} \epsilon}{f_0^2(\infty) Pr} E_3(\tau) \zeta \right] \\ & + \frac{1}{4 f_0(\infty)} \left[\frac{1}{4 f_0(\infty)} \left(\frac{2\phi_{0w}}{f_0(\infty) Pr} E_3(\tau) \xi + \frac{5}{4} \frac{\phi_{0w} \epsilon}{f_0^2(\infty) Pr} E_2(\tau) \zeta \right) \right] \\ & + \frac{1}{4 f_0(\infty)} \left[\frac{1}{16 f_0^2(\infty)} \frac{5\phi_{0w} \epsilon}{f_0(\infty)} E_2(\tau) \zeta \right]. \end{aligned} \tag{23}$$

Equations (20) and (23) must now be expanded for small values τ and then expressed in terms of the inner variable so that the inner and the outer solutions may be joined. For the exponential integral functions one has

$$\left.\begin{aligned} E_2(\tau) \sim 1 - o(\tau), \quad E_3(\tau) \sim 0{\cdot}5 - \tau + \ldots, \\ E_4(\tau) \sim \tfrac{1}{3} - \tfrac{1}{2}\tau + \tfrac{1}{2}\tau^2 + \ldots, \end{aligned}\right\} \quad \text{as} \quad \tau \to 0. \tag{24}$$

Applying (24) and (6) plus the relationship $\tau = \eta\kappa_p\delta$ to (20) and (23), the outer solutions take the form

$$h \sim \frac{\phi_{0w}}{f_0(\infty)\,Pr}\xi + \frac{\phi_{0w}\epsilon}{f_0(\infty)}5\left(\frac{1}{4f_0(\infty)\,Pr} - \eta\right)\zeta \tag{25}$$

and

$$s \sim \frac{\phi_{0w}}{2f_0^2(\infty)Pr}\frac{\xi}{3\kappa_p\delta} + \frac{\phi_{0w}}{4f_0^2(\infty)Pr}\left[\frac{1}{4f_0(\infty)}\left(\frac{1}{Pr}+1\right) - \eta\right]\xi + \frac{5}{8}\frac{\epsilon\phi_{0w}}{f_0^2(\infty)} \times\left[\frac{1}{8f_0^2(\infty)}\left(\frac{1}{Pr}+1\right) - \frac{1}{2f_0(\infty)}\left(\frac{1}{Pr}+1\right)\eta + \eta^2\right]\zeta + \ldots. \tag{26}$$

These relations provide the remote boundary conditions for the inner temperature and velocity functions respectively.

It is noted from (26) that the temperature rise in the outer field induces a velocity of $O(\xi/3\kappa_p\delta)$. The appearance of this parameter is a consequence of the linearization of the equations for the outer region. The parameter is not a function of x and will be referred to as γ, i.e.

$$\gamma = \xi/3\kappa_p\delta. \tag{27}$$

The outer flow thus introduces to the problem an additional perturbation parameter which must be taken into account in the subsequent expansions for the inner field.

This analysis was undertaken to obtain a qualitative understanding of the radiation interaction phenomenon. The number of parameters which arise, even for this simplified treatment, clearly indicates the complexity of the problem. It is interesting to note that the outer radiation driven flow has a characteristic longitudinal velocity of order γ and a characteristic temperature of order ξ, a condition which is very different from that encountered in forced-flow boundary layers with radiation effects.

2.4. *Inner-region solution*

The conservation equations for the inner region are (1)–(3). The velocity is expressed in terms of a stream function and the temperature is generalized as shown below.

$$\psi(x,y) = 5\nu G^* f(\eta,x),$$

$$t - t_0 = \frac{q_{wx}}{kG^*}\,\phi(\eta,x),$$

where $\eta = y/\delta$ is the similarity variable. For the detailed development of these expressions see Sparrow & Gregg (1956). In order to include the effect of radiation interaction, the functions $f(\eta,x)$ and $\phi(\eta,x)$ are expanded in a perturbation series:

$$f(\eta,x) = f_0(\eta) + \zeta f_{11}(\eta) + \xi f_{21}(\eta) + \gamma f_{31}(\eta) + \ldots, \tag{28}$$

$$\phi(\eta,x) = \phi_0(\eta) + \zeta\phi_{11}(\eta) + \xi\phi_{21}(\eta) + \gamma\phi_{31}(\eta) + \ldots. \tag{29}$$

However, before presenting the governing equations for the inner-region stream functions and temperature distributions we shall develop an expression for the

divergence of the radiation flux in this domain. The general expression for a grey non-scattering gas is

$$-\frac{\partial}{\partial\tau}q_{ry} = 2\left[\epsilon\sigma T_w^4 + (1-\epsilon)\,2\int_0^\infty \sigma T^4 E_2(t)\,dt\right]E_2(\tau) + 2\int_0^\infty \sigma T^4 E_1(|\tau - t|)\,dt - 4\sigma T^4. \tag{30}$$

For the optically thin boundary layer and in order to be compatible with the previous outer region approximations, the integrals may be evaluated as follows:

$$\int_0^\infty \sigma T^4 E_2(t)\,dt = \int_0^\infty \sigma T_0^4 E_2(t) + O(\kappa_p \delta) \tag{31}$$

and

$$\int_0^\infty \sigma T^4 E_1(|\tau - t|)\,dt = \int_0^\infty \sigma T_0^4 E_1(t)\,dt + O(\kappa_p \delta). \tag{32}$$

These integrals are accurate to $O(\kappa_p \delta)$ and this order of approximation becomes consistent with the rest of the analysis when (31) and (32) are substituted into the energy equation. The final expression for the divergence of the radiation flux then reads

$$-\partial q_{ry}/\partial t = 2\epsilon\sigma(T_w^4 - T_0^4) - 4\sigma(T^4 - T_0^4) \simeq 8\epsilon\sigma T_0^3(T_w - T_0) - 16\sigma T_0^3(T - T_0). \tag{33}$$

The velocities v and u are defined as

$$u = \frac{\partial}{\partial y}\psi(x,y), \quad -v = \frac{\partial}{\partial x}\psi(x,y).$$

Applying these definitions to (28) and also making use of (29) and (33), the equations for the inner region are as given below, being ordered in terms of powers of the expansion parameters ζ, ξ and γ. The primes refer to derivatives with respect to the similarity variable η.

$$\left.\begin{aligned} \phi'' + Pr\,(f_0'\phi_0 - 4f_0\phi_0') &= 0, \\ f_0''' + 4f_0 f_0'' - 3f_0'^2 &= -\phi_0. \end{aligned}\right\} \tag{34}$$

This first set are the usual boundary-layer equations for non-radiative flows and are subject to the following boundary conditions:

$$\left.\begin{aligned} \phi_0'(0) = -1, \quad \phi_0(\infty) &= 0, \\ f_0(0) = f_0'(0) = 0, \quad f_0'(\infty) &= 0. \end{aligned}\right\} \tag{35}$$

For ζ the following equations and boundary conditions result.

$$\left.\begin{aligned} (1/Pr)\,\phi_{11}'' + 4f_0\phi_{11}' - 3f_0'\phi_{11} + 6\phi_0' f_{11} - f_{11}'\phi_0 &= 40\phi_0 - \epsilon 20\phi_{0w}, \\ f_{11}''' + 4f_0 f_{11}'' - 8f_0' f_{11}' + 6f_0'' f_{11} &= -\phi_{11}, \end{aligned}\right\} \tag{36}$$

$$\left.\begin{aligned} f_{11}(0) = f_{11}'(0) &= 0; \\ \phi_{11}(0) = -20\,Pr\,\epsilon A, \quad \phi_{11}(\infty) &= \frac{\phi_{0w}\epsilon .5}{f_0(\infty)}\left[\frac{1}{4f_0(\infty)\,Pr} - \eta\right], \\ f_{11}'(\infty) = \frac{5}{8}\frac{\phi_{0w}\epsilon}{f_0^2\infty)}\left[\frac{1}{8f_0^2(\infty)}\left(1+\frac{1}{Pr}\right) - \frac{1}{2f_0(\infty)}\left(1+\frac{1}{Pr}\right)\eta + \eta^2\right]. \end{aligned}\right\} \tag{37}$$

For ξ the results are

$$\left.\begin{aligned}(1/Pr)\,\phi''_{21}+4f_0\phi'_{21}-2f'_0\phi_{21}-f'_{21}\phi_0+5\phi'_0 f_{21}=0,\\ f'''_{21}+4f_0f''_{21}-7f'_0f'_{21}+5f''_0f_{21}=-\phi_{21};\end{aligned}\right\} \tag{38}$$

$$\left.\begin{aligned}\phi'_{21}(0)=4\phi_{0w},\quad \phi_{21}(\infty)=\phi_{0w}/f_0(\infty)\,Pr,\\ f_{21}(0)=f'_{21}(0)=0,\\ f'_{21}(\infty)=\frac{\phi_{0w}}{4f_0^2(\infty)\,Pr}\left[\frac{1}{4f_0(\infty)}\left(\frac{1}{Pr}+1\right)-\eta\right].\end{aligned}\right\} \tag{39}$$

For γ we have

$$\left.\begin{aligned}(1/Pr)\,\phi''_{31}+4(f_0\phi'_{31}+f_{31}\phi'_0)-f'_{31}\phi_0-f'_0\phi_{31}=0,\\ f'''_{31}+4(f_0f''_{31}+f_{31}f''_0)-6f'_0f'_{31}=-\phi_{31},\end{aligned}\right\} \tag{40}$$

$$\left.\begin{aligned}\phi'_{31}(0)=\phi_{31}(\infty)=0,\\ f_{31}(0)=f'_{31}(0)=0,\quad f'_{31}(\infty)=\phi_{0w}/2f_0^2(\infty)\,Pr.\end{aligned}\right\} \tag{41}$$

The above boundary conditions at $\eta\to\infty$ are obtained from the outer solution, equations (25) and (26), written in terms of the inner variable η. At $\eta=0$, however, the temperature boundary conditions are obtained as follows. Recall that

$$\left.\frac{\partial t}{\partial y}\right|_{y=0}=-\frac{q_w}{k}+\frac{q_{ry}}{k}. \tag{42}$$

The radiation flux at the wall may be expressed as

$$q_{ry}(0)\simeq 4\epsilon\sigma T_0^3\left[(T_w-T_0)-2\int_0^{\kappa_p\delta}(T-T_0)\,E_2(t)\,dt\right]. \tag{43}$$

Now, expressing (43) in terms of the generalized temperature function ϕ and substituting in (24) for $E_2(t)=E_2(\kappa_p\delta\eta)$ one obtains

$$q_{ry}(0)=4\epsilon\sigma T_0^3\Delta t_c(\phi_{0w}+\zeta\phi_{11}(0)+\xi\phi_{21}(0)+\gamma\phi_{31}(0)-2\kappa_p\delta A+\ldots), \tag{44}$$

where

$$A=\int_0^1\phi_0\,d\eta. \tag{45}$$

Substituting (44) into (42) then gives

$$\phi'_{0w}+\zeta\phi'_{11}(0)+\xi\phi'_{21}(0)+\gamma\phi'_{31}(0)+\ldots=-1+4\phi_{0w}\xi-20\,Pr\,\epsilon A\zeta+\ldots. \tag{46}$$

It might be of value at this point to outline the physical implications of the above analysis. The inner layer, adjacent to the heated surface, has strong velocity and temperature gradients. In the outer layer, heat transport is mainly by convection and radiation. The unperturbed inner boundary-layer region appears to the outer flow as a porous surface with a suction velocity v_0, the heat emitted by this surface being convected back towards it with convection velocity v_0. This causes a temperature rise and consequently a velocity increase at the outer edge of the inner region.

2.5. *Parameter discussion*

In what follows some restrictions imposed on the solution by the parameters will be examined. Consider first the parameter γ, which may be rewritten as

$$\gamma=\xi/3\kappa_p\delta=\epsilon/12N,$$

where $N = k\kappa_p/4\sigma T_0^3$. If $k/4\sigma T_0^3$ is defined as a characteristic conduction length δ_c for transfer problems involving radiation, then N may be written as $N = \kappa_p \delta_c$, a more convenient form for the problem at hand. In order to relate ϵ to the absorption characteristics of the gas one may then write

$$\epsilon = 12(\kappa_p \delta_c)^b = 12N^b$$

and hence

$$\gamma = (\kappa_p \delta_c)^{b-1} = (\kappa_p \delta_c)^m.$$

The requirement $b > 1$ then assures $\gamma < 1$ for decreasing values of the gas absorptivity.

The inner variable η may now be expressed in terms of the expansion parameters as the following:

$$\eta = \frac{\tau}{\kappa_p \delta} = \frac{\tau}{\gamma^{1/m}\delta/\delta_c} = \frac{\tau}{(3\delta/\delta_c)^{m/b} \times \frac{1}{3}\zeta^{1/b}} = \frac{\tau}{10\,Pr\,(\delta_c/\delta)\,\zeta}.$$

Since the wall emission term $4\sigma T_0^3 \epsilon(T_w - T_0)$ appears directly in the inner region energy equation, terms of order $\zeta\epsilon$ are included in the analysis. The equations are solved for different values of ϵ. However, since the optically thin approximation excludes terms of $O(\kappa_p \delta)$ the inclusion of the above terms of $O(\zeta\epsilon)$ becomes questionable for small values of ϵ.

Further, the above solution is valid only when the suction velocity v_0 dominates the outer convection flow. This requires that $\gamma < \kappa_p \delta$. If this condition is not met, the momentum and energy equations for the outer flow may not be decoupled. With the exception of the data taken at the lowest pressure level, and for the highest emissivity surface, our experimental conditions satisfy this condition on γ.

3. Solutions of equations

A fourth-order Runge–Kutta scheme was used to integrate the equations for the inner field, i.e. (34)–(41), the integration being started at the surface. The second derivative of the stream function and the value of the temperature function were guessed and corrected until the far-field boundary conditions were met to within 1×10^{-4}. The method of correction is the familiar one used for two-point boundary-value problems and the Prandtl number used was 0·902, the average value for ammonia for the conditions of the experiment.

The temperature and velocity functions obtained are presented in figures 2 and 3, respectively. As may be seen from (36) and (37), the value of ϵ appears as a parameter in the equations and in the boundary conditions for ϕ_{11} and f_{11}. Its effect on these functions may be seen in the figures. This dependence will be further discussed when the experimental results are presented. The solutions of ϕ_{11} and f_{11} shown for $\epsilon = 0$ represent the case where terms of $O(\epsilon\zeta)$ have been omitted from the analysis.

The solutions in figures 2 and 3 show several interesting characteristics. The radiation correction functions are all negative at small η and thus predict a lowering of the wall temperature. This behaviour results from the added energy transport from the wall and from the hot gas adjacent to the wall by radiation.

The solutions furthermore predict an increase in the temperature in the outer region of the boundary layer due to absorption of the wall-emitted radiation flux in the outer field. In figure 3 it is seen that the general effect of radiation interaction upon the velocity distribution is to lower the velocity in the inner part of the boundary layer and to increase it in the outer part. This is expected from the

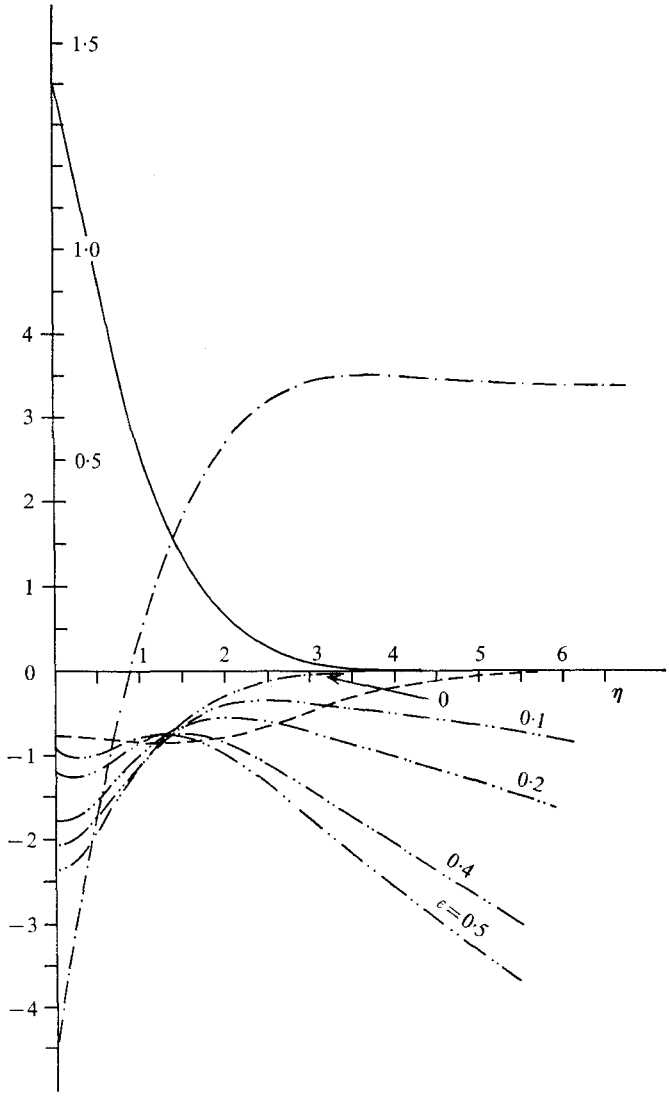

FIGURE 2. Theoretical solutions for the temperature functions. ——, ϕ_0 (inner scale); —··—, $\phi_{11} \times 10^{-1}$; —·—, ϕ_{21}; – – –, ϕ_{31}.

behaviour of the temperature functions. Note that the function ϕ_{31} in figure 2 is the effect upon the inner region temperature distribution of the radiation-induced increase in velocity in the outer region of the boundary layer. Finally, we see that the conditions at the outer edge of the boundary region are dominated by the radiation phenomenon. This is in agreement with previous arguments and

also with published analyses of other workers investigating the forced-flow case (see Viskanta 1966).

In the following sections the experimental apparatus and techniques will first be described, followed by a presentation and discussion of the theoretical and experimental results. The analytical predictions are compared with experimental findings and it is shown that gaseous radiation is a significant transport process for the many applications characterized by the parameters of the present experiment.

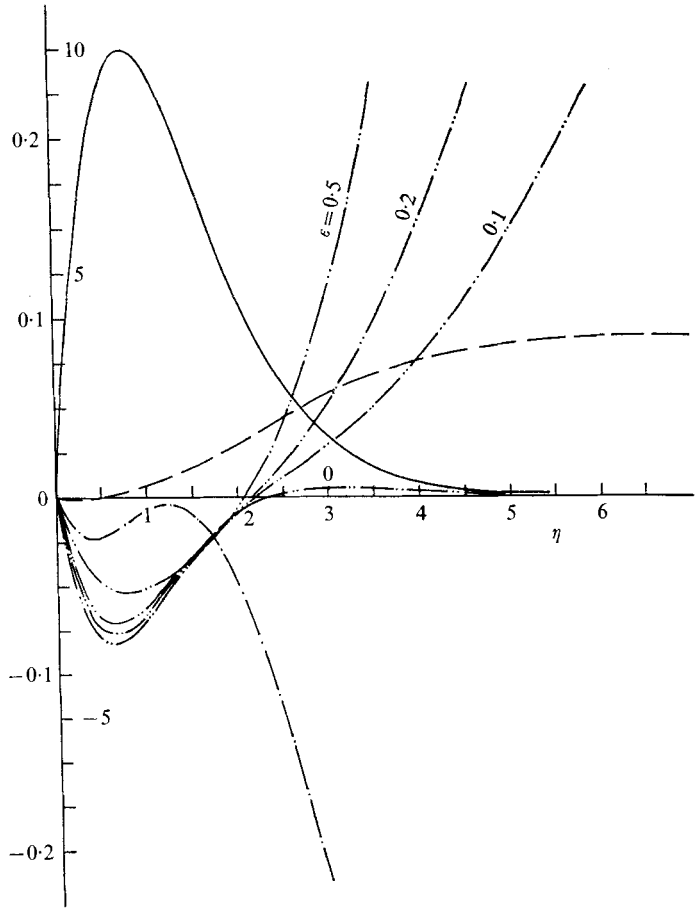

FIGURE 3. Theoretical solutions for the velocity functions. ——, f_0'; —··—, f_{11}' (inner scale); —·—, f_{21}'; – – –, f_{31}' (inner scale).

4. Experiment

4.1. *Experimental apparatus*

The experiment was designed to generate natural convection flow along a vertical flat surface, subject to a uniform heat-flux boundary condition. An electrically heated surface was made from 0·00127 cm thick Inconel-600 foil, 16·51 cm wide and 38·1 cm long. This foil was stretched between two accurately ground knife-edges which were adjusted to make it very flat. Both knife-edges were mounted

vertically to ensure a symmetric flow on the two sides of the vertical foil and were spring-loaded to compensate for any variations in the foil length due to temperature changes.

The foil assembly was held in an adjusting mount to facilitate alignment of the foil in the 20 cm aperture of a Mach–Zehnder interferometer. The foil was aligned vertically using a plumb-bob as a reference. The entire foil assembly was contained inside a large T-shaped test chamber capable of sustaining pressures up to 18 atm. The test chamber had a height of 76 cm, an inside diameter of 35 cm and an optical path length between windows of 69 cm. The test section inside the vessel could be observed through 2·5 by 20 cm wide horizontal slits which were covered by interferometer quality glass windows 5·08 cm thick, 5·08 cm high and 22·5 cm wide. No compensating chamber was necessary since a 7·5 mW helium–neon laser was used as the light source for the interferometer. A description of this interferometer has been given by Gebhart & Knowles (1966).

The interferograms were recorded, by a Graflex camera, on Royal Pan photographic plates. A dimensional reference was needed to scale the pictures correctly. A rod with an accurately machined square-tooth pattern was used for this purpose. In addition, a square grid of fine wire was used to assess any optical distortions due to peripheral optics. All of these measures were necessary to permit the quantitative interpretation of the interferograms in order to determine both the temperature fields and gradients. Both the square-toothed rod and the fine wire grid were located at the edge of the foil.

The resistance of the foil and the foil current were used to determine the total heat flux from the surface. The d.c. current through the foil was measured with a Leeds and Northrup 0·1 Ω resistor. An integrating digital voltmeter ($\pm$ 0·01 % accuracy) was used for this measurement. The resistance of the foil, which was measured prior to the experiments for each foil, was found to vary by less than 0·3 % over the range of heating rates applied and was therefore considered constant. The current through the foil was also monitored by a recorder. The electrical power was obtained from a regulated power supply.

The Mach–Zehnder interferometer yielded interferograms which were used to determine the temperature distribution in the boundary layer. A direct evaluation (see appendix B) of the fringe pattern was made possible by the presence of two calibrated thermocouple junctions, made from 0·00254 cm wire, in the boundary layer and in the interferometer field. Their differential output was measured on a digital voltmeter and monitored by a recorder. The two thermocouple wires were stretched across the width of the foil so that the two wires formed an X, with the junctions in the middle, approximately 0·89 cm apart, normal to the surface. The wire support prongs were 0·159 cm Pyrex glass tubes, through which the wires were run from binding posts. The glass prongs were springy enough to permit a slight bending when the wires were mounted in order to compensate for any variation in wire length due to temperature changes. The thermocouple arrangement is shown in figure 4. Typically, the innermost thermocouple junction was approximately 0·1 cm away from the surface of the plate.

For the first experiments in air and argon, cromel–constantan wires were used. It was found, however, that the cromel reacted with ammonia gas, so for later

runs iron–constantan was used. The wires were calibrated in a temperature-regulated oil bath, where the temperature could be determined to within 0·03 °C. The calibration curves were found to agree to better than 1 % with the standard calibration tables for the respective thermocouple materials.

The ambient temperature in the pressure vessel was measured with a stainless-steel-clad iron–constantan thermocouple placed so that it was effectively shielded from the plate radiation. An ice bath was used for a reference temperature and a digital voltmeter was used to measure the output from the thermocouple. The

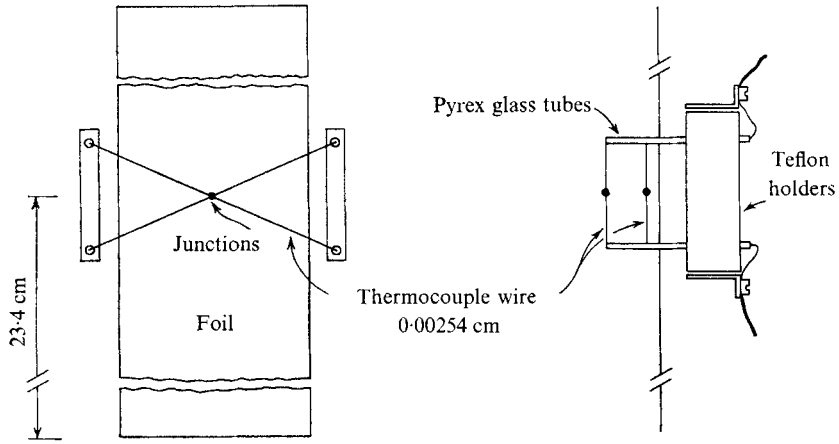

FIGURE 4. Boundary-layer thermocouple arrangement.

pressure in the test chamber was measured with a Heise precision gauge calibrated up to 20 atm. All gases were taken from high-pressure tanks and fed via a pressure-reducing valve into the test chamber. Care was taken to seal the chamber, and the pressure drop was typically about 1 % in 24 h. The interferometer and other test equipment occupies a separate insulated room, without windows, to maintain slowly varying ambient conditions.

4.2. *Experimental procedure*

Experimental data were taken with three different foils surfaced for different emittance values. One set of experiments used the foil in its 'shiny as delivered' surface condition, with an emittance taken from Gubareff, Janssen & Torborg (1960) equal to 0·2. For the second set of measurements the foil surface was covered with a 0·00030 cm thick layer of colloidal graphite. The application of the graphite layer was performed at the Lockheed Missile and Space Center, where the emittance was measured to be 0·5. The last series of data were taken with a foil covered with a layer of black Krylon lacquer about 0·0033 cm thick. Again, from Gubareff *et al.*, and also from interferometer measurements, the emittance was estimated to be 0·80. Extreme care was taken when mounting these foils to avoid fouling or altering the surface in any way.

After a foil had been prepared and placed in the pressure vessel the pressure was raised to the desired value and the gas was allowed several hours to equilibrate with the ambient temperature. When ammonia or argon was used the tank was

filled to 5 atm and purged four times in succession to remove residual gases before the final charge was introduced.

The runs for any given gas and foil were made starting from the highest pressure. For air and argon this was around 8 atm and for ammonia it was between 6 and 7 atm. The power through the foil was adjusted so that the number of fringes formed was approximately twenty for all gas densities. Too high a heating rate resulted in unacceptable refraction of the light rays passing through the boundary layer close to the plate. On the other hand a high number of fringes was desired to minimize the errors due to imperfections in the interferometer optics, and to give good resolution in the calculation of the temperature gradient near the surface. For all runs the interferometer was adjusted to the infinite fringe field condition. This adjustment allows continuous inspection for any stratification or eddy current effects inside the pressure vessel, and furthermore permits fast and accurate location of the foil centre-line. All interferograms were obtained with the camera focused on the thermocouple junctions. These were located in a plane half-way across the span of the foil.

After applying the foil current, the time to reach steady-state conditions could be observed on the recorded output from the boundary-layer thermocouples. The regime of the starting natural convection flow is a true convection transient according to the theory given by Gebhart (1963). The typical transient time for the conditions of these experiments is calculated by the formulation of Gebhart, Dring & Polymeropoulos (1967) to be approximately 15 s. The observed transient times were from 10 to 20 s. After steady-state conditions had been achieved data were taken. To check the reproducibility, two or three sets of data were taken at each pressure setting. The recorded quantities were current, voltage from boundary-layer thermocouples, voltage from the 'ambient-temperature thermocouple', the tank pressure, a picture of the distance scale, a picture of the thermocouple junctions and an interferogram. All runs were made either late at night or in the early morning hours to ensure quiet conditions.

4.3. *Physical properties*

The following physical properties are required: the thermal conductivity $k(p,t)$, the viscosity $\mu(p,t)$, the specific heat $c_p(p,t)$, the density $\rho(p,t)$, the coefficient of thermal expansion $\beta(t)$, the refractive index $n(p,t)$ and the Planck mean absorption coefficient $\kappa_p(p)$, where p is the ambient pressure. All properties except β and κ_p, which were evaluated at ambient temperature, were evaluated at

$$t = t_0 + 0{\cdot}62(t_w - t_0). \tag{47}$$

A detailed discussion concerning property determination is given in appendix A.

4.4. *Data evaluation*

The temperature profiles and the conduction (convection) heat loss from the foil surface were obtained from the interferograms. The quantities measured (on an optical comparator of $\times$ 20) were the spatial distribution of fringes, the number of fringes between the boundary-layer thermocouple junctions, and the distance scale. The exact location of the foil was found to be best established by locating

the midpoint between the two innermost fringes on each side of the foil. This could be done since there were always an equal number of fringes on the two sides.

The distance scale, obtained from the photographs focused on the square-toothed rod, was corrected for the change in magnification which resulted when the focal plane was moved to the plane in which the thermocouple junctions were located. The correction was calculated to be $-2\,\%$. The ratio between real distances and distances on the interferogram was then found to be $0{\cdot}606 \pm 0{\cdot}5\,\%$.

In order to evaluate the exact number of fringes it was necessary to extrapolate from the fringe closest to the foil to the foil surface. The technique employed was similar to the one used by Mollendorf & Gebhart (1970). The fringes closest to the foil were correlated in location by a polynomial regression technique. Good accuracy from the technique is assured by the regular fringe distribution close to the foil, as demonstrated by the interferogram in figure 15 (plate 1). The polynomial correlation permitted extrapolation of the fringe distribution from the innermost fringe to the foil surface and hence the total number of fringes could be determined. The same polynomial correlation was used to find the slope of the fringe distribution at the surface, thus permitting the calculation of the surface conduction (convection mechanism) heat flux.

The evaluation of interferograms for a two-dimensional temperature field as in the present experiment is quite simple in principle. The equation which relates temperature change or specific volume change to fringe shift, using the Dale–Gladstone constant and the ideal gas assumption, is

$$\frac{\Delta t}{N} = \frac{R\lambda T_0^2}{WK(1-(NR\lambda T_0/WKp))} \tag{48}$$

or,

$$\frac{\Delta V}{N} = \frac{\lambda V_0^2}{KW(1-(N\lambda V_0/KW))}, \tag{49}$$

where Δt is the temperature difference and ΔV is the specific volume difference represented by N, the corresponding number of fringes. Also, R is the gas constant, λ is the wavelength of the interferometer light source, K is the Dale–Gladstone constant, W is the length of the optical path in the disturbed region, T_0 is the absolute temperature of the ambient fluid medium and V_0 refers to the specific volume of the ambient fluid medium. For ammonia the specific volume differences were converted to temperature differences with the aid of a virial equation of state. A complete discussion of the equations used for reducing the interferometer data is given in appendix B.

The data for the temperature distributions were normalized in accordance with the definition of $\phi(\eta, x)$. The characteristic quantities are thus computed from the wall heat flux and from the flux Grashof number. The total wall heat flux (convective plus radiative) is used when the data is compared with the analytical predictions for radiative flows. The data, however, were also normalized using only the convective heat flux to compute the characteristic quantities. This was done to obtain a clearer picture of the effect of radiation upon convection in absorbing and non-absorbing media.

The local heat-transfer parameter $Nu/Gr^{\frac{1}{4}}$ was calculated using the convective

heat flux obtained from the interferograms. (See (B 4) or (B 5) in appendix B.) Here $Gr = (g\beta\Delta t_w x^3)/\nu^2$ is the local Grashof number, $Nu = hx/k$ is the local Nusselt number, Δt_w is the local temperature difference across the convection region and h is the convection coefficient. For ammonia gas the change in the wall gradient with gas opacity was also calculated. The presentation and discussion of these results will be the subject of § 5.2.

5. Experimental results and observations

5.1. *Non-absorbing gas*

For a heated radiating surface subject to a uniform-flux boundary condition, an increase in the radiation level at the surface decreases the convection heat flux. A consequence of this alteration of the wall condition is the loss of similarity for the convection process. For natural convection flow along a vertical flat surface, with no heat loss by radiation ($\xi = 0$), the surface temperature varies as the fifth root of the longitudinal distance x. With surface radiation, the wall temperature in the limit of large ξ, i.e. radiation dominant, no longer varies longitudinally. This is a consequence of the uniform-flux boundary condition. However, for the experiments reported herein this extreme condition is not reached.

The experimental results obtained for the non-radiating gases air and argon are displayed as data points in figures 5, 6, 7 and 8, together with calculated curves. These curves were obtained by numerical integration of the equations given by Cess (1964*b*) for $Pr = 0{\cdot}708$ and $Pr = 0{\cdot}675$. These are the typical Prandtl numbers for air and argon for the conditions of the present experiments.

Temperature distributions. As mentioned previously, the experimental temperature data is normalized with a characteristic temperature $\Delta t_c = qx/kG^*$. For a non-radiating surface the heat flux q in this expression is equal to the total wall heat flux. With surface emission the total surface flux becomes $q = q_w = q_r + q_c$, where q_w, q_r and q_c denote, respectively, the measured total, the radiative, and the measured convective heat fluxes at the surface. With radiation present, therefore, normalization with Δt_c based on q_w will illustrate the general reduction of the temperature level resulting from the additional transport mechanism. However, a temperature distribution normalized with Δt_c based on q_c will indicate the effect of the radiation transport, through the boundary condition, on the convection process. Stated differently, it will show the degree of coupling between the two transport mechanisms.

The experimental data points for the temperature distribution were thus generalized with Δt_c based on both q_c and q_w. The resulting distributions are shown in figures 5 and 6 for $\epsilon = 0{\cdot}5$ and figure 7 for $\epsilon = 0{\cdot}8$ as a function of the generalized variable $\eta = y/\delta = yG^*/x$. All experiments were performed at a fixed longitudinal position x. Variations in ξ for a given gas and given ϵ were achieved by changing the pressure.

Considering first the data normalized with Δt_c based on q_w, the results in figures 5, 6 and 7 show a general qualitative agreement with the calculated distributions over this range of the parameter ξ. The discrepancy between the

perturbation solution and the experimental findings is seen to increase steadily with increasing ξ. However, this is to be expected since only one term is included in the expansion around the non-radiative condition. The inconsistancy in the experimental result for $\xi = 0{\cdot}098$ with respect to the other experimental data in figure 7 (i.e. lowest values of ϕ rather than highest) may have been caused by a temperature effect on the emittance of the surface at this lowest wall temperature.

Turning next to the temperature data normalized with Δt_c based on the measured q_c one observes, from these same figures, that as ξ varies from 0·0575 to 0·125 the measured temperature distribution deviates very little from the

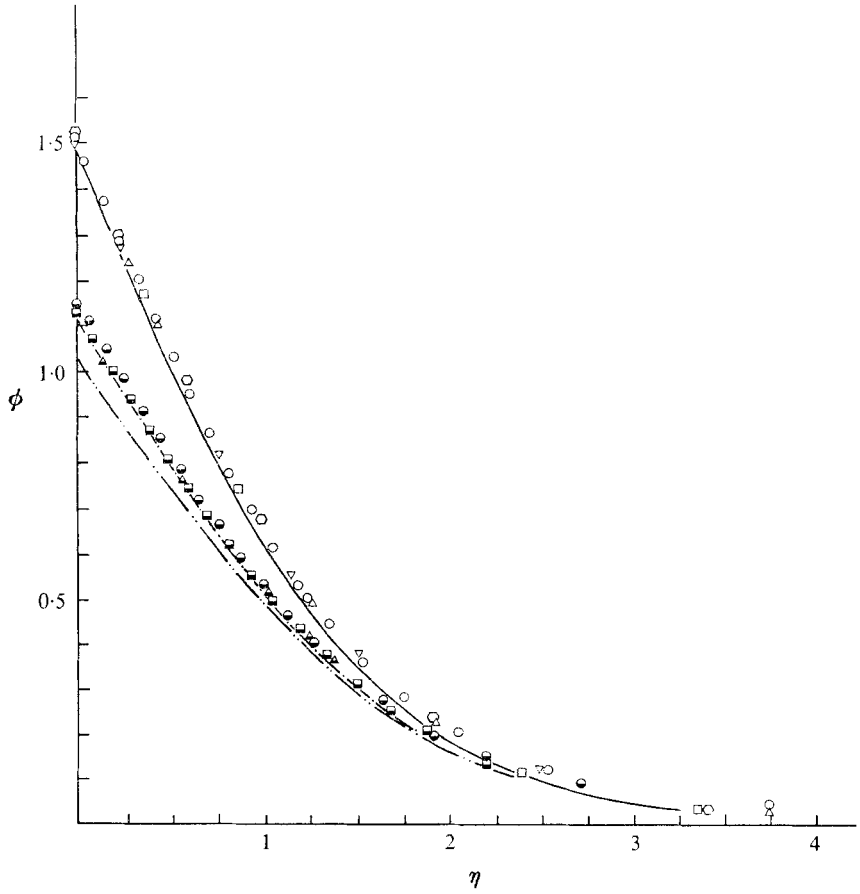

FIGURE 5. Temperature distribution in air, $\epsilon = 0{\cdot}5$, average $Pr = 0{\cdot}708$, ambient temperature for all runs: $T_0 = 297{\cdot}2$ °K. Unfilled points, Δt_c based on q_c; half-filled points, Δt_c based on q_w. Theoretical solutions: —·—, $\xi = 0{\cdot}0575$; —··—, $\xi = 0{\cdot}07$; ——, $\xi = 0$.

Experimental data points	p (atm)	Δt (°C)	ξ
□	3·04	29·4	0·070
⬡	3·04	32·7	0·069
▽	4·02	19·3	0·068
△	6·04	12·2	0·057
○	7·7	10·3	0·0575

pure convection profile calculated for a uniform flux surface. This observed behaviour suggests that the coupling between the radiation and the convection phenomenon is very weak, at least for the conditions of these experiments. Regarding the two processes as being independent and superimposed therefore,

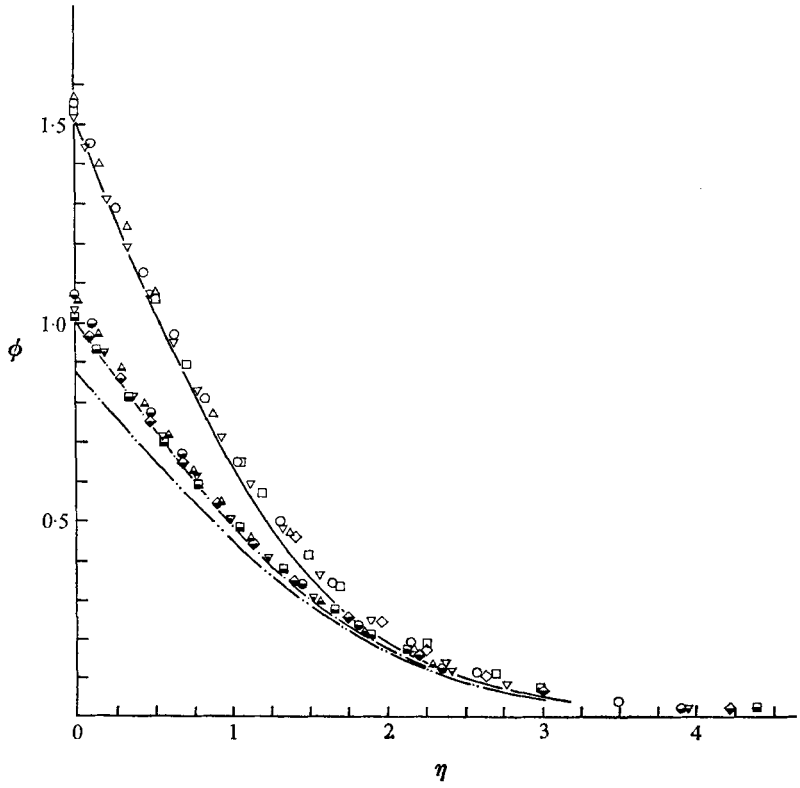

FIGURE 6. Temperature distribution in argon, $\epsilon = 0{\cdot}5$, average $Pr = 0{\cdot}675$, ambient temperature for all runs: $T_0 = 294{\cdot}7$ °K. Unfilled points, Δt_c based on q_c; half-filled points, Δt_c based on q_w. Theoretical solutions: —···—, $\xi = 0{\cdot}094$; —·—, $\xi = 0{\cdot}075$; ——, $\xi = 0$.

Experimental data points	p (atm)	Δt (°C)	ξ
□	3·04	30·6	0·094
◇	3·04	33·4	0·092
▽	4·03	23·9	0·087
△	6·02	17·5	0·075
○	7·6	10·5	0·075

one arrives at the following approximate equation for the reduction in temperature when radiation transfer is present:

$$\phi(\eta_r) = [1 - \tfrac{16}{5}\xi\phi_r(0)]\phi_0(\eta), \tag{50}$$

where

$$\phi_r(0) = \phi_0(0)/[1 + \tfrac{16}{5}\xi\phi_0(0)] \tag{51}$$

and

$$\eta_r = \eta_0/(1 - 4\xi\phi_r(0))^{\frac{1}{4}}. \tag{52}$$

The subscripts 0 and r refer to the pure convection and the convection–radiation condition respectively. These expressions permit direct calculation of the effect

of surface radiation on the surface temperature and boundary-region temperature distribution, based upon the known solutions for non-radiative flows. Table 1 compares values of $\phi_r(0)$, calculated from (51) and from the perturbation solution, with experimental results for various values of ξ.

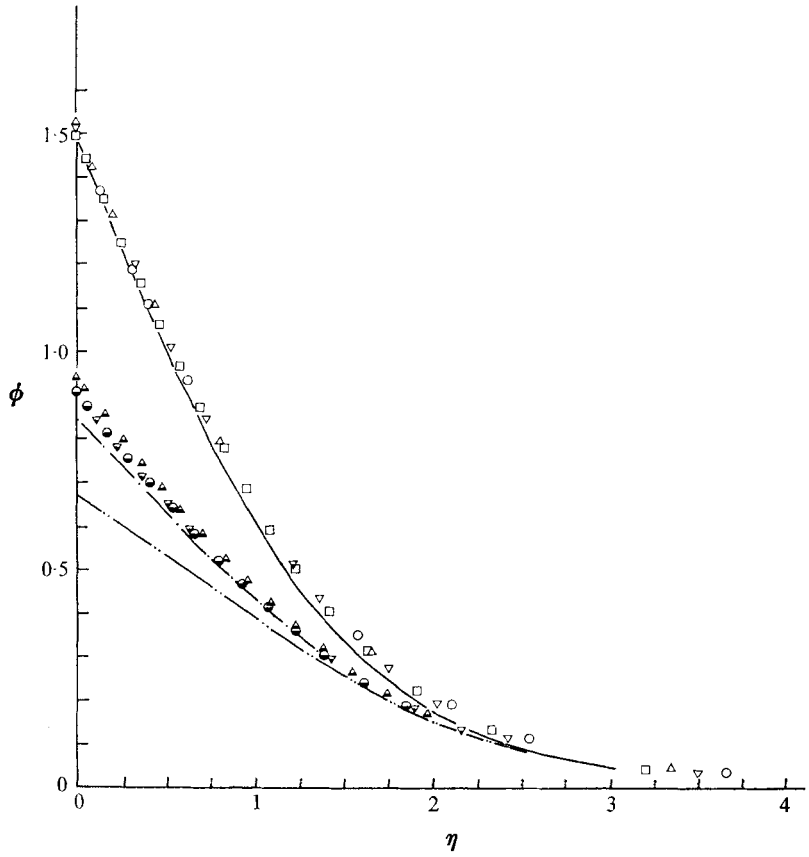

FIGURE 7. Temperature distribution in air, $\epsilon = 0{\cdot}8$, average $Pr = 0{\cdot}708$, ambient temperature for all runs: $T_0 = 299{\cdot}7$ °K. Unfilled points, Δt_c based on q_c; half-filled points, Δt_c based on q_w. Theoretical solutions: —··—, $\xi = 0{\cdot}125$; —·—, $\xi = 0{\cdot}098$; ——, $\xi = 0$.

Experimental data points	p (atm)	Δt (°C)	ξ
▽	2·02	38·9	0·125
△	3·04	29·6	0·111
□	4·05	20·9	0·104
○	6·06	11·7	0·098

The suggested approximate technique is seen to agree to within 4% with the experimental values of $\phi_r(0)$.

Heat-transfer results. The convective heat-transfer data are shown in figure 8. The abcissa is ξ and the ordinate is $NuF(Pr)/Gr^{\frac{1}{4}}$, where $F(Pr) = \phi_0(0)^{\frac{5}{4}}\, 5^{\frac{1}{4}}$. That is, the Prandtl number effect as calculated from boundary-layer theory is used to normalize the data. This comparison indicates that the trend of the experimental data is in agreement with the result calculated by Cess (1964*b*). The spread

of the data around the faired (or estimated average) curve drawn through the data points is approximately 2 %. The experimental results are seen to be consistently above the theory. The magnitude of the difference, however, is too small to distort the impression of general agreement.

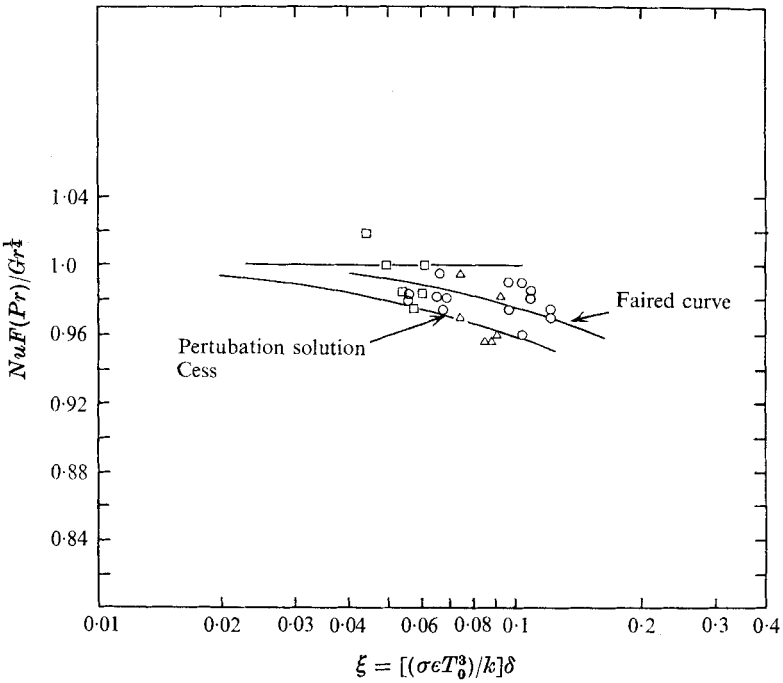

FIGURE 8. Convective heat-transfer data for air and argon.
□, Cess data. Present data: ○, air; △, argon.

ξ	Experiment $\phi_r(0)$	Cess $\phi_r(0)$	Equation (51)	ϵ
0·0575	1·15	1·11	1·17	0·5
0·07	1·13	1·03	1·12	
0·075	1·07	1·01	1·11	
0·094	1·02	0·877	1·04	
0·104	0·956	0·810	1·00	0·8
0·125	0·904	0·673	0·934	

TABLE 1. Comparison of the experimental values of the normalized surface temperature with the values predicted by the Cess (1964*b*) perturbation solution and (51)

5.2. *Absorbing gas*

We next consider the experimental temperature distributions and heat-transfer results measured for natural convection flow in NH_3 gas. Figures 9, 10 and 11 show temperature distributions for three different levels of surface emittance, normalized with Δt_c based on q_c. In figures 12, 13 and 14 the same data have been normalized with Δt_c based on q_w and are compared with our numerical solution.

In figure 15 (plate 1, an interferogram) the thickness of one particular radiating boundary layer is compared with the corresponding non-radiative case. Finally, figures 16 and 17 compare both the theoretically and experimentally determined wall temperature gradients and heat-transfer parameters. Again, all of the data were obtained at a fixed longitudinal position at various values of ambient pressure.

Temperature distribution. As discussed earlier, the temperature data normalized with Δt_c based on q_c indicate the degree of coupling between the radiation and convection transport processes in the gas. By considering figures 9, 10 and 11, it may be seen that the decreasing level of the experimental data, with increasing

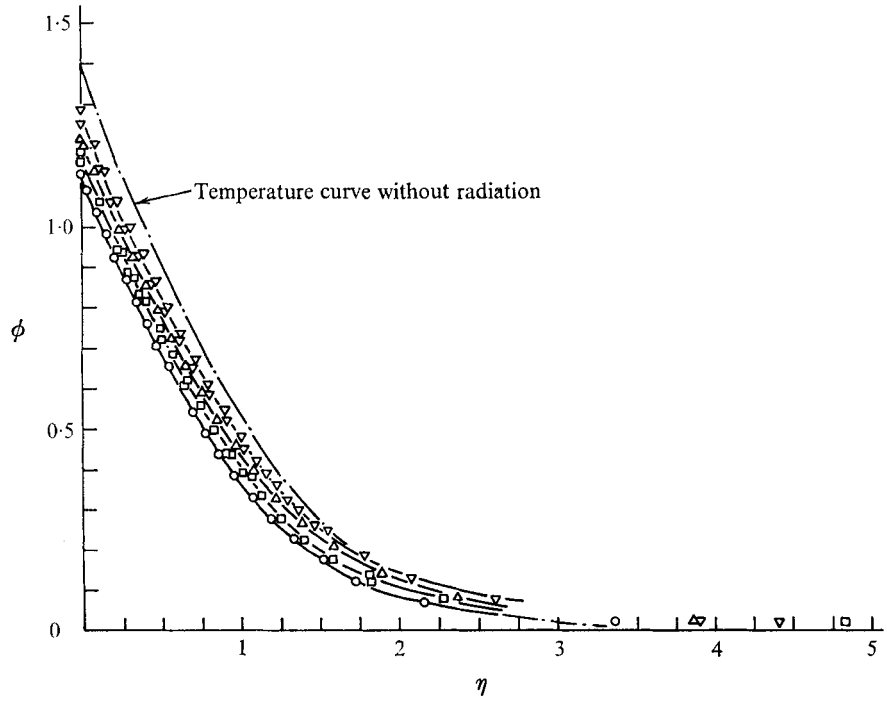

FIGURE 9. Temperature distribution in ammonia gas, $\epsilon = 0{\cdot}2$, Δt_c based upon q_c, average $Pr = 0{\cdot}902$, ambient temperature for all runs: $T_0 = 298{\cdot}6$ °K. Note that the data points have been connected with faired curves.

Experimental data points	p (atm)	Δt (°C)
▽	2·02	37·8
△	3·11	19·5
□	4·1	14·4
○	6·03	8·73

opacity of the boundary layer (high pressures), offers evidence of strong radiation–convection interaction. This may be seen by contrasting the above results with either the previously discussed experimental results for the non-absorbing gases at various pressures or with the temperature curve without radiation, shown in each figure for comparison. The observed behaviour may perhaps be best understood by considering the nature of optically thin radiation. As indicated by (33), the gradient of the radiation flux changes sign from positive to negative as the

boundary layer is traversed. Thus one concludes that there is a gain in radiative flux through the hot layer of gas adjacent to the surface, implying that the gas is mainly emitting. Stated differently, the optically thin radiation provides a form of 'short circuit' in the energy transport through the boundary layer. A consequence of this effect is the observed lowering of the normalized temperature level. The regular increase in the normalized temperature with decreasing values of pressure, corresponding to decreasing values of the boundary-layer opacity ($\kappa_p \delta$ or the parameter ζ), is consistent with this argument.

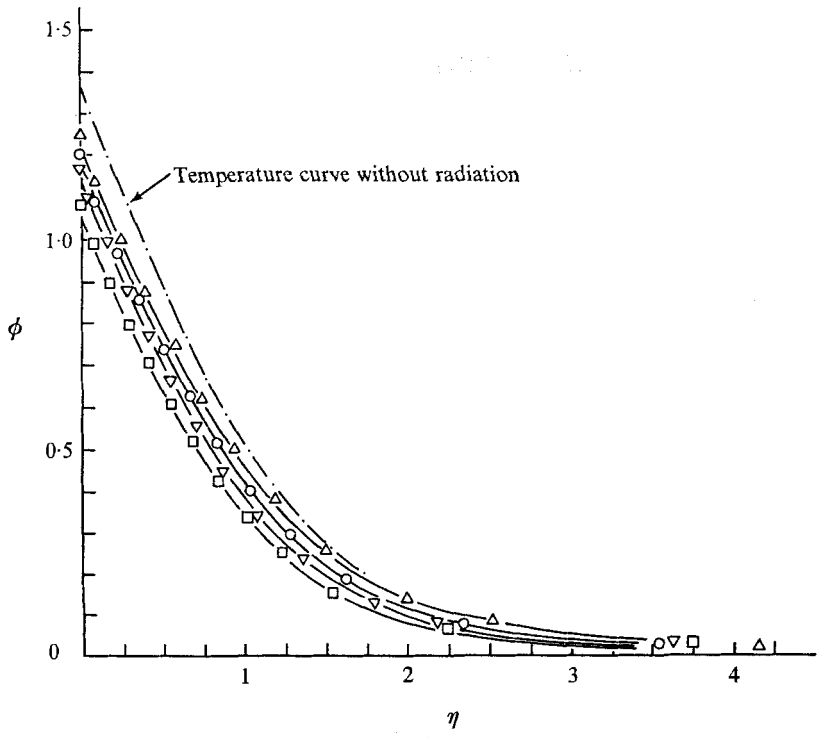

FIGURE 10. Temperature distribution in ammonia gas, $\epsilon = 0{\cdot}5$, Δt_c based upon q_c, average $Pr = 0{\cdot}902$, ambient temperature for all runs: $T_0 = 294{\cdot}7\,^\circ\mathrm{K}$.

Experimental data points	p (atm)	Δt (°C)
△	3·1	20·6
○	4·1	14·4
▽	6·0	8·73
□	6·8	7·74

The optically thick limit is often assumed in analysis and it is interesting to consider the above data from this point of view. In its simplest form the radiation transport in a grey gas may be treated as an added diffusion process. The radiation effect may consequently be accounted for by an augmented thermal conductivity, and the convection process occurs as if it were taking place at a lower Prandtl number. Recall that the non-radiative curve is the limit for both the totally opaque and the totally transparent radiation–convection phenomenon. From the approximate relation $\phi(0) \propto Pr^{-\frac{1}{2}}$, the value of $\phi(0)$ decreases as the Prandtl

number increases. This suggests that the totally opaque limit is approached from a higher value of $\phi(0)$ than in the non-radiative case. The present results, however, show $\phi(0)$ decreasing (figures 9, 10 and 11) for increasing pressure. One may extrapolate this trend and heuristically argue that $\phi(0)$ could continue through a minimum before, in the totally opaque limit, returning to the pure convection form. This argument, however, contradicts the behaviour predicted from the

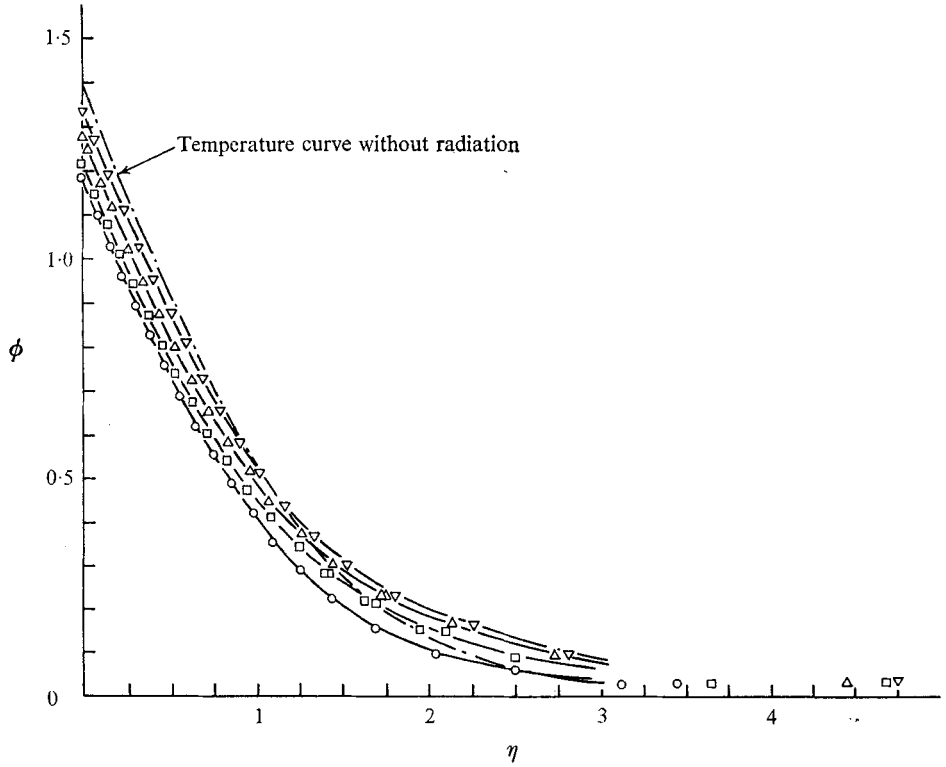

FIGURE 11. Temperature distribution in ammonia gas, $\epsilon = 0{\cdot}8$, Δt_c based on q_c, average $Pr = 0{\cdot}902$, ambient temperature for all runs: $T_0 = 299{\cdot}7$ °K. (Note: ± 5 % uncertainty in —○— data.)

Experimental data points	p (atm)	Δt (°C)
▽	2·03	32·20
△	3·07	19·10
□	4·10	13·43
○	6·03	7·12

optically thick approximation. Novotny & Yang (1967) observed a similar contradiction for the optically thick approximation in their analytical study of radiation interaction in a natural convection stagnation flow for an optically thick gas. They found that an exact solution predicted that the wall temperature gradient approached the opaque limit while decreasing, whereas the optically thick diffusion approximation indicated the opposite trend. The similarity between these observations is striking. Both results demonstrate the failure of the diffusion approximation near the surface.

The same measured temperature distributions are shown in figures 12, 13 and

14 with Δt_c based on q_w. As previously discussed, this normalization of temperature data includes the total effect of the wall-emitted radiation flux upon the temperature distribution. Also included in these figures are the calculated distributions obtained for values of the expansion parameters corresponding to the conditions of our experiments. The temperature distribution in the absence of any radiation effect has again been included for reference.

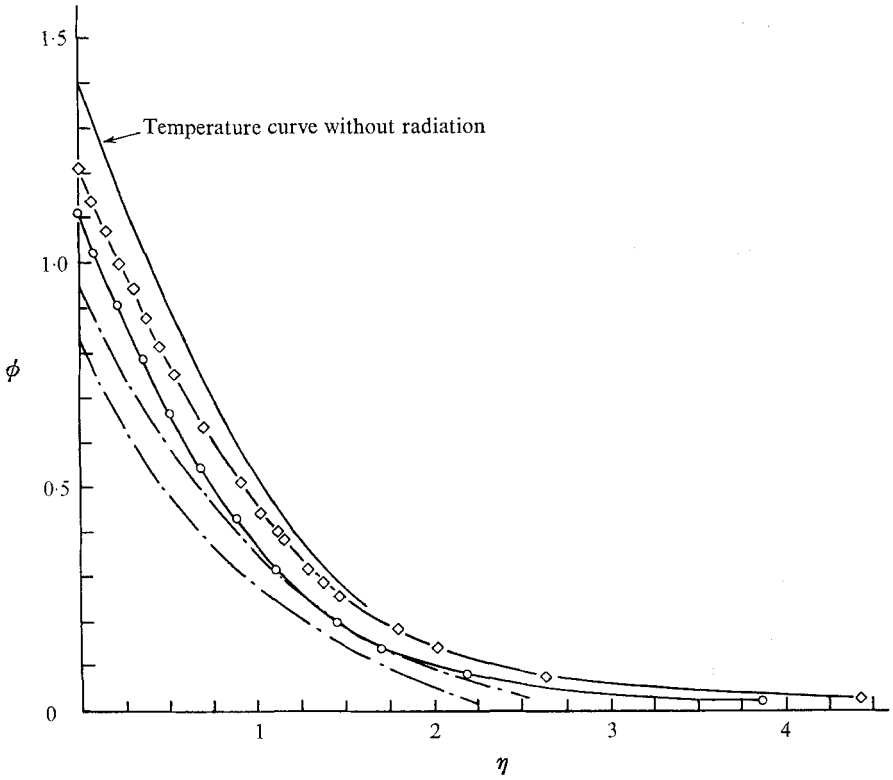

FIGURE 12. Temperature distribution in ammonia gas, $\epsilon = 0{\cdot}2$, Δt_c based upon q_w, average $Pr = 0{\cdot}902$, ambient temperature for all runs: $T_0 = 298{\cdot}6\,°\text{K}$. Note that the data points have been connected with faired curves.

p (atm)	Δt (°C)	ζ	ξ	γ	Experimental data points	Present theoretical solution
2·02	37·8	0·0141	0·0342	0·0604	–◇–	—·—
6·03	7·78	0·0241	0·0252	0·0192	–○–	—··—

In figure 12, for $\epsilon = 0{\cdot}2$, only the data obtained at 6·03 atm and 2·02 atm are shown. Measurements at intermediate pressures fall between these results. The quantitative agreement between theory, the dashed lines, and experiment, the points, is seen to be approximately 20 %. Considering, however, that only first-order terms are included in the perturbation expansion and, perhaps more important, that the gas is assumed grey, this discrepancy is not unreasonable. There is qualitative agreement and the theory predicts the correct general behaviour and trends. The above discrepancy between theoretical and observed

behaviour decreases with higher wall emittance. As discussed previously, this may result from the increased significance of terms of $O(\zeta\kappa_p\delta)$ for small values of wall emittance. It is important to note that for this low value of the wall emittance the measured and calculated non-dimensional temperature levels decrease with increasing values of the parameter ζ (or pressure). Similar behaviour is seen in figures 9, 10 and 11. This indicates that the effect of gaseous radiation dominates the effect of surface emission. We recall that for non-absorbing gases increased pressure (ξ decreasing) resulted in a higher non-dimensional temperature level.

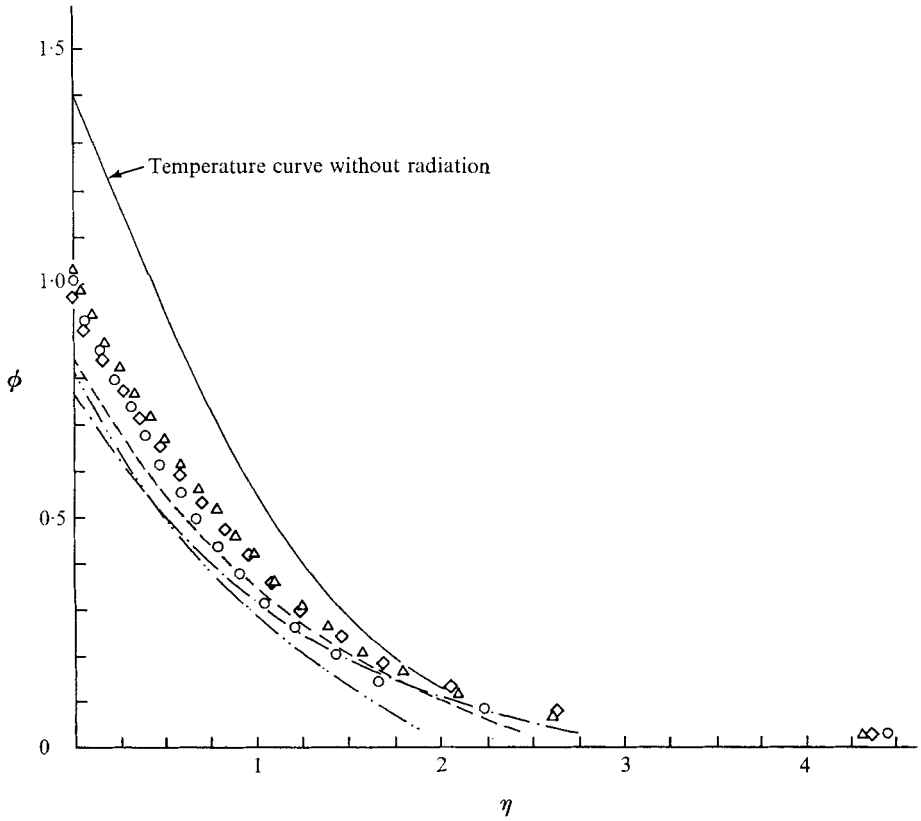

FIGURE 13. Temperature distribution in ammonia gas, $\epsilon = 0{\cdot}5$, Δt_c based upon q_w, average $Pr = 0{\cdot}902$.

p (atm)	T_0 (°K)	Δt (°C)	ζ	ξ	γ	Experimental data points	Present theoretical solution
3·1	294·7	20·6	0·0156	0·0720	0·099	△	———
2·02	298·6	26·65	0·0100	0·0844	0·157	◇	—·—
6·86	298·6	5·84	0·0275	0·0625	0·0416	○	—··—

Experimental results shown in figure 13 for 0·5 wall emittance include data obtained at two different ambient temperatures, namely $T_0 = 298{\cdot}6$ °K and $T_0 = 294{\cdot}7$ °K. For $T_0 = 298{\cdot}6$ °K data obtained at 6·86 and 2·02 atm are shown. Data obtained at intermediate pressures (4·02 and 3·1 atm) fall between these

distributions. For $T_0 = 294{\cdot}7\,^\circ\mathrm{K}$ the distribution obtained at 3·1 atm is included to illustrate the effect of lowering the ambient temperature. Data obtained at higher pressures (4, 6·07 and 6·7 atm) fall systematically above the presented distribution.

Comparing the measurements for $\epsilon = 0{\cdot}5$ at $T_0 = 298{\cdot}6\,^\circ\mathrm{K}$ with those for $\epsilon = 0{\cdot}2$ at the same ambient temperature, it is seen that the increased wall emittance results in a lower temperature level in the boundary region. The large effect resulting from increased wall emission also demonstrates the optically thin

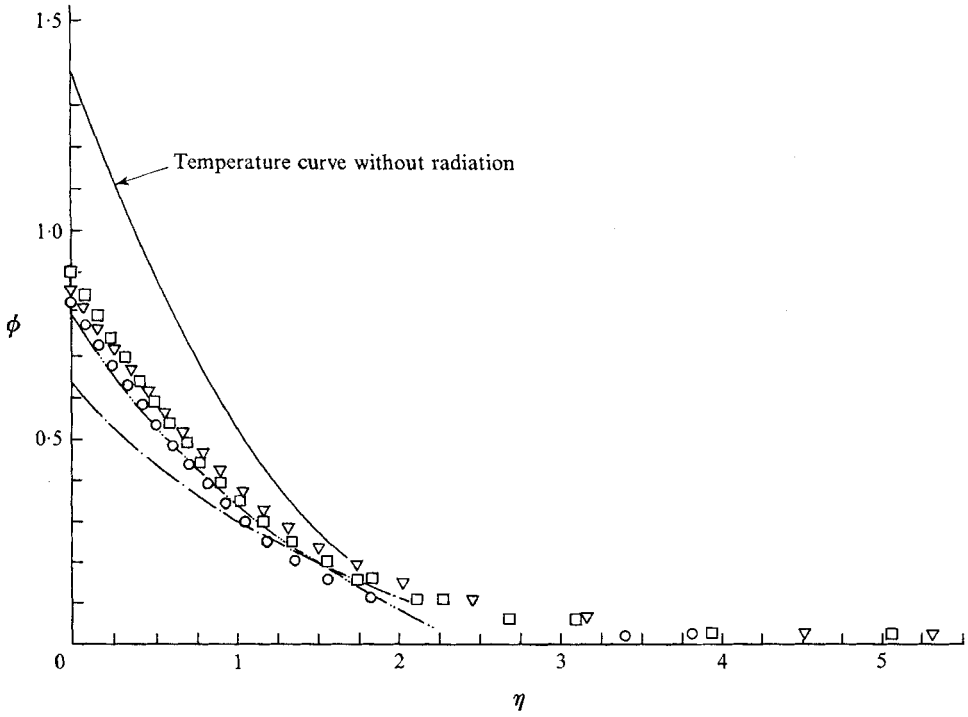

FIGURE 14. Temperature distribution in ammonia gas, $\epsilon = 0{\cdot}8$, Δt_c based upon q_w, average $Pr = 0{\cdot}902$, ambient temperature for all runs: $T_0 = 299{\cdot}7\,^\circ\mathrm{K}$.

p (atm)	Δt (°C)	ζ	ξ	γ	Experimental data points	Present theoretical solution
2·03	32·2	0·0131	0·131	0·238	▽	—·—
4·10	13·43	0·0193	0·113	0·122	□	—··—
6·03	7·12				○	

nature of these boundary layers. The wall temperature now increases with increasing pressure, in contrast to the observations for $\epsilon = 0{\cdot}2$. That is, the radiation interaction phenomenon is more strongly governed by the variations in the surface emission. The quantitative agreement between measured and calculated behaviour is similar to that for $\epsilon = 0{\cdot}2$, and again there is good qualitative agreement. In terms of expansion parameters, we see that the increase in gaseous radiation, as characterized by the increase in ζ with pressure, is not sufficient to counteract the effects of the combined decrease in ξ and γ. The solution for ϕ_{11}

in figure 2 also indicates that the 'surface cooling effect' of an absorbing and emitting gas is reduced when the wall emittance is increased. The physical reason is that more gaseous radiation is absorbed by the surface, rather than being reflected back into the gas.

Consideration of the data for 3·1 atm and $T_0 = 294{\cdot}7\,^{\circ}\mathrm{K}$ indicates that the reduction in ambient temperature increases the boundary-layer temperature level. This is expected, since lowering the ambient temperature, with other conditions remaining the same, results in a decrease in the overall radiation intensity. The qualitative agreement between the observed and predicted behaviour is again good.

The highest surface emittance used in this experiment was $\epsilon = 0{\cdot}8$ and the measured temperature profiles are shown in figure 14. The increase in wall emittance further decreases the generalized temperature level, compared with the distributions in figures 12 and 13. With exception of the data obtained at 6·03 atm the behaviour of these temperature distributions is consistent with the previous observations and conclusions. The measured and calculated non-dimensional temperature levels increase as the pressure increases, i.e. ζ increases and ξ and γ decrease. The temperature distribution obtained at 6·03 atm, however, is too low. Similar behaviour, again at the highest pressure or lowest surface temperature, was also observed for the air data presented in figure 7. The same foil was used for that experiment. The present behaviour, therefore, may again be explained by an increase in the wall emittance at this the lowest surface temperature.

As previously discussed, it is implied in the analysis [see equation (20)] that the far-field non-dimensional temperature level is porportional to ξ, i.e. the radiant emission from the surface. Considering separately each wall emittance, the temperature data for large η ($\eta > 2$ say) corroborates this analytical prediction. For example, one notes that for $\epsilon = 0{\cdot}5$ (figure 13) the highest temperature level for $\eta > 2{\cdot}0$ corresponds to the largest value of the parameter ξ (note the crossing of the temperature distributions as the boundary layer is traversed). On the other hand, a comparison of the far-field temperature levels as obtained for the different wall emittances does not show a change in magnitude comparable to these variations in ξ. The quantitative discrepancy is consistent with the grey-gas assumption and the omission of higher-order terms in the perturbation expansion. We do find, however, an increase in the boundary-layer thickness with ξ (or ϵ), indicating qualitative agreement with predicted behaviour.

The boundary-layer quality of the natural convection flow in this radiating gas is perhaps best illustrated by the interferogram in figure 15 (plate 1). This interferogram was obtained for a wall emittance of 0·8, at 2·02 atm. The 'edge' of the corresponding non-radiative boundary layer, indicated in the figure, represents the same fraction of $\phi(0)$ (with Δt_c based either on q_c or q_w) as the outermost fringe in the interferogram.

The present experimental technique of varying the pressure to change the experimental parameters makes it possible to contrast the gaseous radiation effect with the effect of wall emission. The two effects increase and decrease respectively with pressure. The experiment thus also constitutes a severe test of the analytical predictions.

Finally, it will be pointed out that, unless stated otherwise, the uncertainty in the above data, as judged by their repeatability, is of the order of 2 %.

Heat-transfer results. The effect of gaseous radiation upon heat-transfer and wall-temperature gradient is perhaps the matter of most practical interest; the experimental and theoretical values for these quantities are given below. In figure 16 the data for the surface temperature gradient, as obtained for different

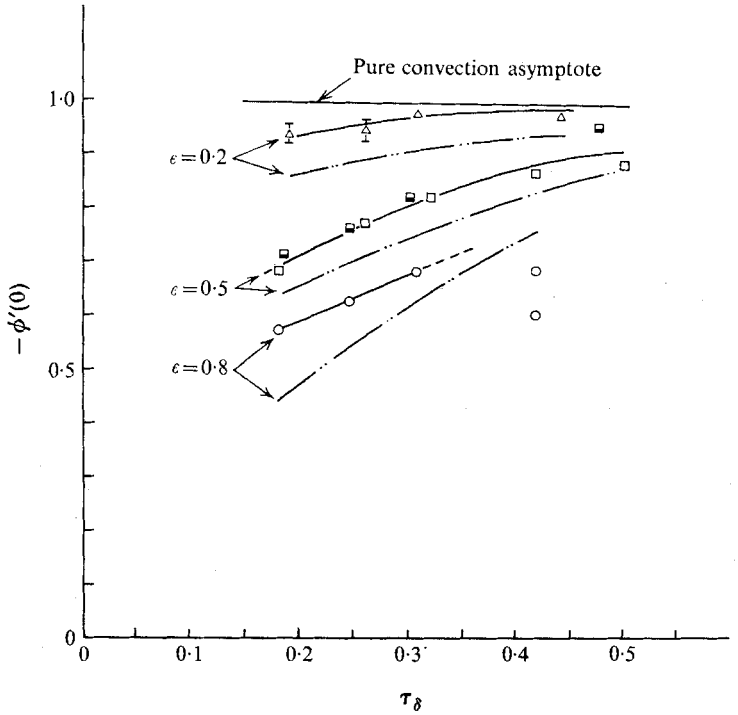

FIGURE 16. Variation of wall-temperature gradient with boundary-layer opacity and surface emittance. The half-filled square data points for $\epsilon = 0{\cdot}5$ were obtained at $T_0 = 294{\cdot}7\,^\circ\mathrm{K}$ and have been corrected to make them comparable to the unfilled data points obtained at $T_0 = 298{\cdot}6\,^\circ\mathrm{K}$. ——, faired experimental curve; —·—, present theory.

values of the wall emittance, are plotted against the optical thickness of the boundary layer ($\tau_\delta = \kappa_p \delta$). The temperature gradient at the surface is found from the analysis to be

$$-\phi'(0) = \begin{cases} 1+\zeta 3{\cdot}36-\xi 5{\cdot}57, & \epsilon = 0{\cdot}2, \\ 1+\zeta 8{\cdot}40-\xi 5{\cdot}57, & \epsilon = 0{\cdot}5, \\ 1+\zeta 13{\cdot}4-\xi 5{\cdot}57, & \epsilon = 0{\cdot}8. \end{cases} \tag{53}$$

These relations are included in the figure. The abscissa is obtained by calculating the values of τ_δ corresponding to different values of ζ and ξ for each wall emittance.

The agreement between calculated and observed behaviour is reasonably good. The decrease in the gradient with increasing τ_δ is a consequence of the increased amount of gaseous radiation absorbed by the surface. To the present order of approximation, this is being conducted back into the gas. The presence of gaseous

radiation reduces the net surface-emitted radiation flux. The net radiative flux from a wall into a non-absorbing gas can be expressed as

$$\epsilon\sigma(T_w^4 - T_0^4) \sim 4\sigma T_0^3 \epsilon (T_w - T_0).$$

Consequently one may express the net radiative flux into an absorbing gas as $4\epsilon'\sigma T_0^3(T_w - T_0)$. In this expression ϵ' is a corrected emittance, which accounts for the presence of an absorbing and emitting gas at a temperature different from T_0. The ratio ϵ'/ϵ may be derived from the analysis, using (53) and the relationship $q_r = q_w - q_c$, to be

$$\frac{\epsilon'}{\epsilon} = 1 - \frac{\zeta}{\xi}\frac{D}{4\phi_0(0)} + \ldots, \tag{54}$$

where $D = 20\epsilon Pr A$ and $A = 0{\cdot}931$ is defined by (45). This relation allows a direct calculation of the heat loss by emission in an absorbing gas. Some experimental and calculated values of ϵ'/ϵ are shown in table 2. The experimental uncertainty in these data is large since the result is the difference between large numbers. This difference is especially small when $\epsilon = 0{\cdot}2$.

	ϵ'/ϵ			
ζ/ξ	Equation (54)	Experiment	ϵ	Estimated uncertainty
0·95	0·42	0·22	0·2	50 %
0·412	0·752	0·350	0·2	50 %
0·440	0·340	0·430	0·5	5 %
0·162	0·756	0·765	0·5	5 %
0·171	0·600	0·740	0·8	5 %
0·100	0·760	0·800	0·8	5 %

TABLE 2. Experimental and calculated values of the effective emissivity of a radiating surface in an absorbing gas

The effect of an absorbing and emitting gas on the local convective heat-transfer parameter, the local Nusselt number based upon the local temperature difference, is calculated as

$$\frac{Nu}{Gr^{\frac{1}{4}}}F(Pr) \sim 1 + \left(-\phi_{11}'(0) - \frac{5}{4}\frac{\phi_{11}(0)}{\phi_0(0)}\right)\zeta - \left(4\phi_0(0) + \frac{5}{4}\frac{\phi_{21}(0)}{\phi_0(0)}\right)\xi - \frac{5}{4}\frac{\phi_{31}(0)}{\phi_0(0)}\gamma + \ldots \tag{55}$$

or

$$\frac{Nu}{Gr^{\frac{1}{4}}}F(Pr) \sim 1 + A(\epsilon)\zeta + B\xi + C\gamma, \tag{56}$$

where the various quantities, calculated for $Pr = 0{\cdot}902$, are given in table 3.

One notes that $A(\epsilon)$ decreases with increasing ϵ, whereas B and C remain constant. Thus, a decrease in the heat-transfer parameter is predicted for increasing ϵ, resulting from both the decrease in $A(\epsilon)$ and from the increase in ξ. For any given surface emittance, however, an increase in gaseous radiation (ζ increasing) is predicted by (56) to increase the value of the heat-transfer parameter. The physical arguments underlying this behaviour have already been discussed.

The experimental and theoretical results for the heat-transfer parameter are plotted in figure 17. The faired data curve for non-absorbing gases is also included

for comparison. The abcissa is ξ. Since $\xi \propto p^{-\frac{3}{8}}$, whereas $\zeta \propto p^{\frac{1}{8}}$ and $\gamma \propto p^{-1}$, decreasing values of ξ correspond to increasing values of ζ and decreasing values of γ. The wall emittance ϵ is noted for all data points. Experiments were carried out at two different ambient temperature levels for $\epsilon = 0{\cdot}5$, as indicated in the figure.

ϵ	$A(\epsilon)$	B	C	$\phi_0(0)$	$\phi_{11}(0)$	$\phi_{21}(0)$	$\phi_{31}(0)$
0·0	23·66	−1·67	0·7	1·396	−23·7	−4·40	−0·786
0·1	20·28	−1·67	0·7	1·396	−20·76	−4·40	−0·786
0·2	19·31	−1·67	0·7	1·396	−17·87	−4·40	−0·786
0·25	18·92	−1·67	0·7	1·396	−16·42	−4·40	−0·786
0·4	17·53	−1·67	0·7	1·396	−12·07	−4·40	−0·786
0·5	16·6	−1·67	0·7	1·396	−9·18	−4·40	−0·786
0·8	13·88	−1·67	0·7	1·396	−0·489	−4·40	−0·786

TABLE 3. Constants for the calculation of convective heat transfer

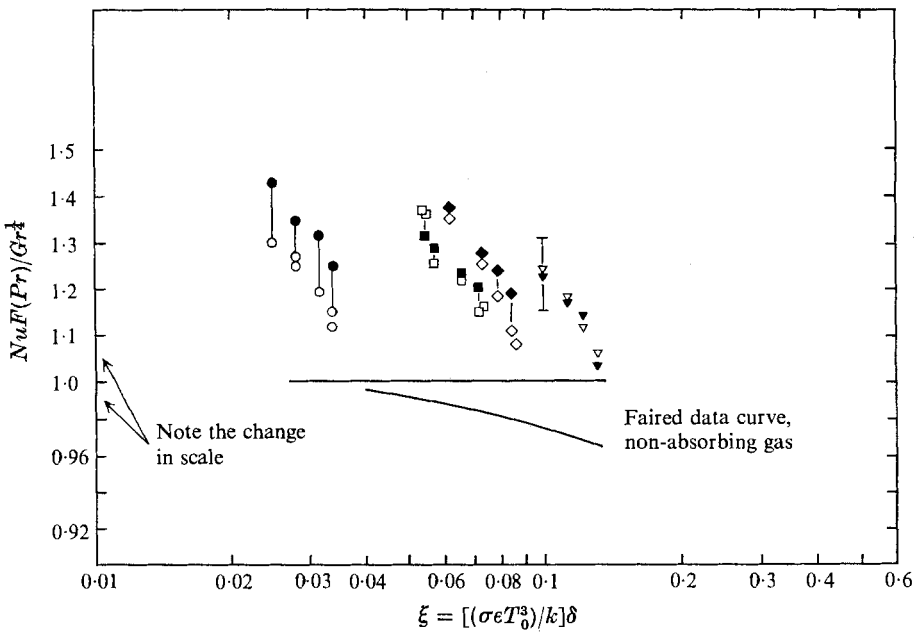

FIGURE 17. Heat-transfer results for ammonia gas. Filled points represent the present theory.

Experimental data points	ϵ	T_0(°K)
○	0·2	298·6
□	0·5	294·7
◇	0·5	298·6
▽	0·8	299·7

Figure 17 shows good qualitative agreement between the experimental and theoretical predictions; the largest discrepancy is of the order of 10%. The changes with ambient temperature in the experimental findings for $\epsilon = 0{\cdot}5$ are in agreement with predicted behaviour. The data, however, exhibit a smaller

increase in the convective heat transfer with decreasing wall emittance than was predicted. This is apparent when comparing the agreement between theoretical and experimental results for $\epsilon = 0{\cdot}2$ with that observed for higher wall emittance. As previously discussed, however, at this low wall emittance the gaseous radiation dominates the interaction phenomena, and the approximate nature of the optically thin gas and grey-gas assumptions have greater effect. For easier comparison of the experimental results at different wall emittances, data for $\phi(0)$, normalized with Δt_c based on q_c, and experimental values of $NuF(Pr)/Gr^{\frac{1}{4}}$ are given in table 4 below.

	$\epsilon = 0{\cdot}2$		$\epsilon = 0{\cdot}5$		$\epsilon = 0{\cdot}8$	
Pressure	$\phi(0)$	$NuF/Gr^{\frac{1}{4}}$	$\phi(0)$	$NuF/Gr^{\frac{1}{4}}$	$\phi(0)$	$NuF/Gr^{\frac{1}{4}}$
2·02	1·26	1·14	1·31	1·10	1·34	1·05
3·1	1·23	1·17	1·24	1·18	1·28	1·11
4·1	1·17	1·27	1·19	1·25	1·22	1·18
6·04	1·13	1·31	1·17	1·29	1·19	1·23

TABLE 4. Average experimental results for the wall temperature and heat-transfer functions

The values of $\phi(0)$ are included since, as may be seen from the definition of ϕ, a relative increase in the convective heat-transfer rate will effect a decrease in the value of $\phi(0)$. Examination of the tabulated results shows a consistent increase in convective heat transfer with decreasing values of ϵ, thus lending support to the predicted behaviour.

It is not surprising that the grey-gas approximation tends to over-estimate the effect of gaseous radiation. The results of Schimmel, Novotny & Olsofska (1970) and of Cess (1964*a*) also show this tendency. The uncertainty of the above experimental heat-transfer data, as judged from their repeatability, is of the order of 3 %.

6. Summary and conclusions

The foregoing results and observations have indicated many interesting aspects of the interaction of infra-red radiation with a natural convection flow adjacent to a vertical surface for both absorbing and non-absorbing gases. For non-absorbing gases the observed weak coupling between the radiation and the convection processes indicates that the two transport mechanisms may be regarded as superimposed. The effect is only in boundary conditions and the convection transport may be formulated as a non-radiative process. The perturbation parameter ξ expresses the effect of surface emission on boundary conditions and the present experimental measurements agree well with the resulting theory. We note that, although the analysis is nominally valid only for $\xi < 1$, the result has the correct asymptotic behaviour for large ξ in that the wall temperature becomes uniform.

However, the absorbing gas ammonia causes a strong interaction between radiation and convection, shown by both the analysis and the experimental results. From the measured temperature distributions the magnitude and nature of the gaseous radiation interaction was found. The results indicate that these boundary layers may be regarded as optically thin, implying little self-absorption within this region. For an optical thickness ($\kappa_p \delta$) of the boundary layer equal to 0·44 it was found that gaseous radiation decreases the non-dimensional temperature level by approximately 20 %. The optically thick radiation approximation, which for a grey gas treats the radiation transfer as a diffusion process, was shown to result in incorrect predictions when compared with the experimental behaviour.

The temperature data clearly indicate the nature of the effects of radiation on the boundary-layer temperature levels. General agreement was found between the analysis and the data. The measurements show that the net effects of gaseous radiation interaction vary strongly with the emission and absorption characteristics of the surface generating the flow. For example, for $\epsilon = 0{\cdot}2$ an increase in the ambient pressure, under the conditions of the present experiment, resulted in a decrease in the non-dimensional surface temperature. However, for $\epsilon \geqslant 0{\cdot}5$ a similar increase in the ambient pressure led to an increase in the non-dimensional surface temperature. This characteristic is predicted by the theoretical solution. The temperature gradient at the surface is strongly influenced by the effect of gaseous radiation and absorption. Compared with a non-absorbing gas, we find that gaseous radiation effect may decrease the negative surface gradient by a factor of two for our present experimental conditions. The theoretical solution predicts a similar effect.

An important question in the present investigation is the influence of gaseous radiation upon the total and the convective heat transfer. For the ammonia gas used in the present experiment the convective heat transfer increased from 6 to 40 %, depending upon the wall emittance and the magnitude of the characteristic quantities associated with the gaseous radiation phenomenon. The theory and experimental results are in good general agreement, although the computed effect of decreasing wall remittance ϵ is larger than the observed. However, the trends of the two results agree.

It is interesting that Gille & Goody (1964), in their study of the onset of thermal convection in a radiating gas (ammonia), and Schimmel *et al.* (1970) in their study of pure conduction through a radiating gas (N_2O, CO_2), both predicted and observed increased conductive heat flux at the wall for increased gas pressure. The present decrease in conductive heat flux at the wall with increasing wall emittance was also demonstrated analytically by Gille & Goody (1964). The results of Cess (1964*a*) for forced flow along an isothermal flat plate have this same characteristic.

The total surface heat flux is the sum of the convective (conductive) and the radiative heat fluxes. However, with a radiating gas the net radiation flux emitted by the surface is less than in a non-absorbing gas because of the surface absorption of radiation emitted in the adjacent gas layer. This characteristic is apparent in both analysis and experiment. When evaluating the net effect of gaseous radiation upon the total heat flux, therefore, both the increase in the convective heat flux and the decrease in the surface emitted heat flux must be considered. Thus,

depending upon the fraction each mode represents in the total, gaseous radiation may decrease or increase the total surface heat flux.

The above results clearly demonstrate that gaseous radiation may not be ignored for natural convection processes where the magnitudes of the different parameters become comparable to the present ones.

Unfortunately, the experimental set-up did not permit measurement of the velocity field. However, the interferograms and the measured temperature distributions show that the temperature boundary layer in ammonia gas is thicker than for comparable conditions with a non-radiating gas. This indicates the presence of a radiation-induced outer velocity field in these optically thin conditions.

The agreement between theory and experiment indicates that the analysis contains many of the major features of the phenomenon. The analysis thus served the purpose of providing a basis for the understanding of a rather complex transport process. Although the above results and observations pertain to a particular natural convection circumstance, it is felt that the information will prove useful for other heat-transfer conditions as well. Natural convection along a constant temperature surface is one example. To a certain extent these results may also qualify some of the assumptions and predictions made in the analytical studies of forced-flow radiation interaction phenomena.

The authors wish to acknowledge the support of the National Science Foundation through Grants GK-1963 and GK-18529 for this research, and support from the same grants for the first author as a research assistant. We are also thankful for the suggestions of Dr S. F. Shen, Dr S. Leibovich and Dr C. A. Hieber. The second author also wishes to acknowledge the interesting and helpful conversations with Dr C. L. Tien during the planning for this investigation.

Appendix A. Property evaluation

Air. Apart from the thermal conductivity, all properties of air were interpolated from tabulated values (Eckert & Drake 1959). The thermal conductivity was taken from Kannuluik & Carman (1951), who give k as a function of temperature as

$$k = 2{\cdot}41 \times 10^{-4}(1 + 0{\cdot}003t - 0{\cdot}0000021t^2)\,\mathrm{W/cm\,^{\circ}C}. \tag{A 1}$$

The index of refraction was taken from International Critical Tables (1930). The coefficient of thermal expansion and the density were calculated using the ideal gas relationships.

Argon. The properties for argon were taken from International Critical Tables (1930) and evaluated at the temperature given by (47). The coefficient of thermal expansion and the density were again obtained from the ideal gas laws.

Ammonia. The calculation of physical properties for ammonia follows the same general procedure as that outlined in Gille & Goody (1964). However, some different data sources are used. The following virial equation of state and the first virial coefficient for ammonia were taken from Hirschfelder *et al.* (1954):

$$pV = RT + B(T)(RT/V). \tag{A 2}$$

The specific heat at constant pressure, c_p, was taken from the work of Osborn *et al.* (1925) which in Din (1956) is shown to be in good agreement with spectrographic

data. With c_p known, the value of c_v, the specific heat at constant volume, can be calculated from the equation of state.

The viscosity of ammonia varies greatly with temperature and pressure. For the pressure and temperature range employed in the present experiment only limited detailed viscosity data are available. The viscosity values published by Stakelbeck (1933) have been used here.

With the values of viscosity established one has, according to Chapman & Cowling (1964),

$$k = f\mu c_v, \tag{A 3}$$

where f can be regarded as a constant, in accordance with the work of Mason & Monchick (1962). The value of f used for the present experiment was 1·46. This value was found to give values of the thermal conductivity in good agreement with the experimental findings of Needham & Ziebland (1965).

The index of refraction was taken from International Critical Tables (1930), and the coefficient of thermal expansion was calculated from the ideal gas relationship. κ_p was found graphically from the plots in Hottel & Sarofim (1967) to be $9\,\mathrm{atm^{-1}\,ft^{-1}} \times p$. This data source was recommended by Tien (1968), who found the data to be in agreement with his calculations from spectroscopic measurements.

Appendix B

Evaluation of interferometer data

If K (the Dale–Gladstone constant) and W (the length of the optical path in the disturbed region) are known with sufficient accuracy, then equations (48) or (49) allow a direct calculation of Δt or ΔV from the fringe field. However, in view of the uncertainties in W, which is usually taken to be the width of the surface, of the paucity of data for the index of refraction of ammonia, and the non-ideal behaviour of ammonia, it was decided to determine experimentally the interferometer constant, i.e. the left-hand sides of the following two relations:

$$\frac{R\lambda T_0^2}{WKp} = C_1 = \frac{\Delta t}{N(1+(\Delta t/T_0))} \tag{B 1}$$

for air and argon, and

$$\frac{\lambda V_0}{KW} = C_2 = \frac{\Delta V}{N(1+(\Delta V/V_0))} \tag{B 2}$$

for ammonia. The number of fringes, N, and the corresponding known temperature difference, Δt, between the two boundary-layer thermocouple junctions was obtained directly from the interferograms. Hence C_1 or C_2 could be calculated. (Note that in (B 2) ΔV is related to the measured temperature difference Δt by the virial relation (A 2).) The value of the interferometer constant (C_1 or C_2) was in each case assumed to be invariant through the boundary layer. The temperature profile for air and argon could then be calculated from (48). For ammonia, however, the specific volume distribution was first calculated from (49) and the corresponding temperature profile was found by an iteration technique from

$$\frac{R}{p}\Delta t + \frac{RT_0}{V_0 p} B(T_0)\left\{\frac{(1+(\Delta t/T_0))\,B(T_0+\Delta t)}{(1+(\Delta V/V_0))B(T_0)} - 1\right\} - \Delta V = 0. \tag{B 3}$$

The temperature gradient at the wall was calculated from the wall gradient $\partial N/\partial y$ of the measured fringe distribution. For air and argon the following expression was used:

$$\left.\frac{\partial t}{\partial y}\right|_{y=0} = \frac{T_w}{N}\left(\frac{T_w}{T_0}-1\right)\left.\frac{\partial N}{\partial y}\right|_{y=0}. \tag{B 4}$$

For ammonia, however, the expression becomes more complicated, owing to the non-ideal behaviour of the gas.

$$\left.\frac{\partial t}{\partial y}\right|_{y=0} \frac{p\Delta V[1+(\Delta V/V_0)]\,[1+(RT_w B(T_w)/pV_w^2)]}{RN[1+(T_w/V_w)\,B'(T_w)+(B(T_w)/V_w)]}\left.\frac{\partial N}{\partial y}\right|_{y=0}, \tag{B 5}$$

where $B'(T_w)$ is the derivative of $B(T)$ (the virial coefficient for ammonia) with respect to T evaluated at the wall. Equation (B 4) or (B 5) then allows the calculation of the conductive heat flux at the wall.

Experimental results for the interferometer constant

As was mentioned earlier, the relationship between fringe shift and temperature change was found experimentally to eliminate errors which would result from using nominal values for quantities like the width of the disturbed field and the index of refraction. The experimental repeatability of these measurements at each pressure was approximately $\pm 1{\cdot}5\,\%$ for ammonia and $\pm 1{\cdot}0\,\%$ for air and argon. The findings have been tabulated in table 5.

The invariance of the tabulated results with ϵ suggest that the effect of radiation upon the boundary-layer differential thermocouples is effectively cancelled. They were both located close to the foil surface, thus having approximately equal geometrical view factors to the foil.

Finally, the non-ideal behaviour of the ammonia gas may be seen from the large deviation of the interferometer constant from the theoretical value, at pressures above 4·09 atm.

Gas	Pressure (atm)	Experimental value, normalized to 26·7 °C and 1 atm: $\epsilon_w = 0{\cdot}8$	$\epsilon_w = 0{\cdot}5$	$\epsilon_w = 0{\cdot}2$	Weighted average	Theoretical value
NH_3	6·7	—	2·833	—	2·833	3·319
	6·06	2·822	2·843	2·944	2·863	
	4·09	3·117	3·132	3·118	3·118	
	3·09	3·283	3·268	3·281	3·276	
	2·02	3·500	3·467	3·433	3·407	
Air	7·7	—	4·333	—	4·333	4·362
	6·04	4·199	4·256	—	4·222	
	4·03	4·372	4·389	—	4·379	
	3·04	4·500	4·497	—	4·499	
	2·02	4·574	—	—	4·574	
Argon	7·7	—	4·461	—	4·461	4·533
	6·09	—	4·483	—	4·483	
	4·03	—	4·528	—	4·528	
	3·11	—	4·639	—	4·639	

TABLE 5. Theoretical and experimental values of the interferometer constant ($[\lambda RT_0^2/WKp]$) °C/fringe

REFERENCES

ARPACI, V. S. 1968 Effect of thermal radiation on the laminar free convection from a heated vertical plate. *Int. J. Heat Mass Transfer*, **11**, 871–881.

CESS, R. D. 1964*a* Radiation effects upon boundary layer flow of an absorbing gas. *Trans. A.S.M.E.* C **86**, 469–475.

CESS, R. D. 1964*b* *Advances in Heat Transfer*, **1**, 1–49.

CESS, R. D. 1966 The interaction of thermal radiation with free convection heat transfer. *Int. J. Heat Mass Transfer*, **9**, 1269–1277.

CHAPMAN, S. & COWLING, T. G. 1964 *The Mathematical Theory of Nonuniform Gases.* Cambridge University Press.

DIN, F. (ed.) 1956 *Thermodynamic Function of Gases*, vol. 1. Butterworths Scientific Publications.

ECKERT, E. R. G. & DRAKE, R. M. 1959 *Heat and Mass Transfer*, 2nd edn. McGraw-Hill.

ENGLAND, W. G. & EMERY, A. F. 1969 Thermal radiation effects on the laminar free convection boundary layer of an absorbing gas. *J. Heat Transfer*, **91** (1), 37–44.

GEBHART, B. 1963 Transient natural convection from vertical elements – appreciable thermal capacity. *Trans. A.S.M.E.* C **85**, 10–14.

GEBHART, B. 1971 *Heat Transfer*, 2nd edn. McGraw-Hill.

GEBHART, B., DRING, R. P. & POLYMEROPOULOS, C. E. 1967 Natural convection from vertical surfaces, the convection transient regime. *Trans. A.S.M.E.* C **89**, 53–59.

GEBHART, B. & KNOWLES, C. P. 1966 Design and adjustment of a 20 cm Mach–Zehnder interferometer. *Rev. Sci. Instr.* **37**, 12–15.

GILLE, J. & GOODY, R. 1964 Convection in a radiating gas. *J. Fluid Mech.* **20**, 47–79.

GUBAREFF, G. G., JANSSEN, J. E. & TORBORG, R. H. 1960 *Thermal Radiation Properties Survey*, 2nd edn. Minneapolis: Honeywell Regulator Co.

HIRSCHFELDER, J. O., CURTIS, C. F. & BIRD, R. B. 1954 *Molecular Theory of Gases and Liquids.* Wiley.

HOTTEL, H. C. & SAROFIM, A. F. 1967 *Radiative Transfer.* McGraw-Hill.

KANNULUIK, W. G. & CARMAN, E. H. 1951 The temperature dependence of the thermal conductivity in air. *Aust. J. Sci. Res.* **4**, 305–314.

MASON, E. A. & MONCHICK, L. 1962 Heat conductivity of polyatomic and polar gases. *J. Chem. Phys.* **36** (6), 1622–1639.

MOLLENDORF, J. C. & GEBHART, B. 1970 An experimental study of vigorous transient natural convection. *Trans. A.S.M.E.* C **92**, 628–634.

NEEDHAM, D. P. & ZIEBLAND, H. 1965 The thermal conductivity of liquid and gaseous ammonia and its anomalous behaviour in the vicinity of the critical point. *Int. J. Heat Mass Transfer*, **8**, 1387–1414.

NOVOTNY, J. L. & YANG, K. T. 1967 The interaction of thermal radiation in optically thick boundary layers. *Trans. A.S.M.E.* C **81**, 309–312.

OSBORNE, N. S., STIMSON, H. F., SLIGH, T. S. & CRAGUE, C. S. 1925 *Sci. Paper U.S. Bur. Stand.* no. 501.

SCHIMMEL, W. P., NOVOTNY, J. L. & OLSOFKA, F. A. 1970 Interferometric study of radiation–conduction interaction. *Fourth International Heat Transfer Conference, Paris–Versailles.*

SPARROW, E. M. & GREGG, J. L. 1956 Laminar free convection from a vertical plate with uniform surface heat flux. *Trans. A.S.M.E.* C **78**, 435.

STAKELBECK, VON H. 1933 Über die Zahigkeit Verschiedener Kaltemittel im Fussigen und Dampf-Formigen Zustand in Abhangigkeit von Druck und Temperatur. *Zeitschrift für die gesamte Kälte-Industrie*, **3**, 33–40.

TIEN, C. L. 1968 Thermal radiation properties of gases. *Advances in Heat Transfer*, **5**, 167–248.

VISKANTA, R. 1966 Radiation transfer and interaction of convection with radiation heat transfer. *Advances in Heat Transfer*, **3**, 175–251.

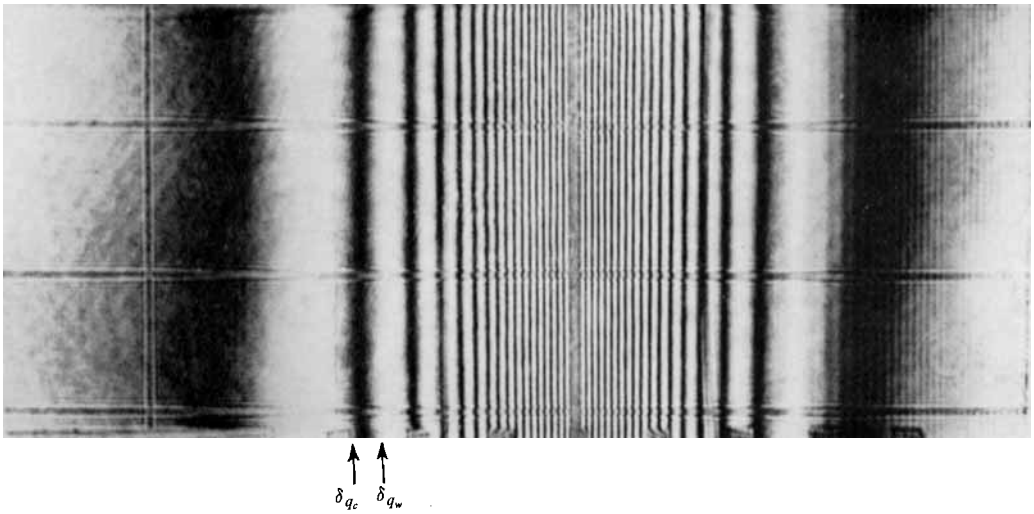

FIGURE 15. Interferogram of boundary layer in ammonia gas, for $\epsilon = 0{\cdot}8$, $p = 2{\cdot}02$ atm, $\Delta t = 32{\cdot}2$ °C, $T_0 = 299{\cdot}7$ °K. δ_{q_c} and δ_{q_w} represent the equivalent edge of a non-radiative boundary layer as compared with the temperature data normalized with Δt_c based on q_c or q_w.